Dissipation-driven formation of entangled dark states in strongly coupled inhomogeneous many-qubit systems in solid-state nanocavities

Mikhail Tokman, Alex Behne, Brandon Torres, Maria Erukhimova, Yongrui Wang, and Alexey Belyanin

Phys. Rev. A **107**, 013721 — Published 27 January 2023

DOI: 10.1103/PhysRevA.107.013721

Dissipation-driven formation of entangled dark states in strongly-coupled inhomogeneous many-qubit systems in solid-state nanocavities

Mikhail Tokman,[1] Alex Behne,[2] Brandon Torres,[2] Maria Erukhimova,[3] Yongrui Wang,[2] and Alexey Belyanin[2]

[1] *Department of Electrical and Electronic Engineering, Ariel University, 40700 Ariel, Israel*
[2] *Department of Physics and Astronomy, Texas A&M University, College Station, TX, 77843 USA*
[3] *No current affiliation*

(Dated: January 3, 2023)

We study quantum dynamics of many-qubit systems strongly coupled to a quantized electromagnetic cavity field in the presence of decoherence and dissipation for both quantum emitters and cavity photons, and taking into account the varying coupling strength of different qubits to the cavity field and the spread of their transition frequencies. Compact analytic solutions for time-dependent quantum state amplitudes and observables are derived for a broad class of open quantum systems in Lindblad approximation with the use of the stochastic Schroedinger equation approach. We show that depending on the initial quantum state preparation, an ensemble of qubits can evolve into a rich variety of many-qubit entangled states with destructive or constructive interference between the qubits. In particular, when only a small fraction of qubits is initially excited, the dissipation in a cavity will inevitably drive the system into robust dark states that are completely decoupled from the cavity and live much longer than the decay time of the cavity field. We also determine the conditions under which coherent coupling to the quantized cavity field overcomes the dephasing caused by a spread of transition frequencies in multi-qubit systems and leads to the formation of a decoupled dark state.

I. INTRODUCTION

Solid-state cavity quantum electrodynamics (QED) attracted much interest as a promising platform for quantum information and quantum sensing systems; see, e.g., [1–5] for recent reviews. A typical scenario involves an ensemble of quantum emitters (ideally, two-level systems) such as quantum dots, defects in crystals, or molecules, strongly coupled to a quantized electromagnetic (EM) field in a dielectric or plasmonic nanocavity. We will call these quantum emitters qubits for brevity, although the logical qubits forming the gates may involve many two-level systems as well as photonic or mixed degrees of freedom. Several or many qubits are required for most applications. Although direct near-field coupling among qubits is possible and desired for some gating protocols, in the nanophotonics context such coupling would require deterministic placement of qubits with sub-nm accuracy, which is challenging. A simpler scenario which still permits various ways of quantum state manipulation is the one in which the qubits are coupled only through the common cavity field. This is the situation considered in this paper.

The problem of N qubits strongly coupled to a quantized cavity mode has been considered many times, starting from the seminal Tavis-Cummings paper [6]. Inherent in most of these studies is the assumption of identical qubits coupled to the field with identical coupling strengths. This makes the system invariant to permutations and allows one to drastically reduce the number of degrees of freedom and related computational effort; see, e.g., the recent work [7] (and references therein) where an efficient numerical solver was proposed to solve the N-qubit master equation in the Lindblad approximation. In the solid-state nanocavity context, the cavity field is strongly nonuniform, especially in plasmonic nanocavities where it varies on a nanometer scale. This makes the qubit-cavity coupling strength strongly variable from qubit to qubit. Moreover, for many popular quantum emitters, such as quantum dots, optically active point defects, excitons in semiconductor nanostructures etc., the spread of transition frequencies exceeds homogeneous linewidth, making inhomogeneous broadening the dominant source of dephasing. Any of these factors break permutation symmetry and increase the complexity of the problem, making it difficult to solve even numerically for large N. As a result, the problems with dissimilar quantum emitters are usually analyzed for few qubits, and even then numerical treatment of the Lindblad master equation is required, e.g., [8–10].

Here we are able to drastically simplify the analysis and obtain analytic or semi-analytic solutions for quantum dynamics of N strongly coupled dissimilar qubits or multilevel fermionic systems in the presence of decoherence and dissipation for both quantum emitters and cavity photons. This progress is made possible by applying a modified version of the stochastic Schrödinger equation (SSE) formalism. The idea of adding Langevin noise to the Schrödinger equation is nothing new; see, e.g., [11–17]. This approach is typically used for numerical Monte-Carlo simulations. We recently developed a version of SSE suitable for analytic solutions of open strongly-coupled cavity QED problems [18, 19] and, as we show here, it is quite useful in analysis of nonuniform and inhomogeneously broadened many-qubit systems. In this paper we focus on the dissipation-driven formation of highly entangled dark states that are decoupled from the cavity field. The ability to generate and control such states is a problem of great practical importance for the rapidly developing field of plasmonic nanocavity QED, where the dissipation of a cavity mode is much faster than the relaxation in quantum emitters [20–25]. The dissipation-driven formation of entangled bright and dark states in ensembles of quantum emitters has been studied extensively in the context of the Dicke model of superradiance [26, 27]; see, for example, [28–34] and references therein. The typical bad-cavity or no-cavity regime of Dicke superradiance is in a sense opposite to the regime of strong-coupling dynamics, although extended samples can still demonstrate complex oscillatory quasi-chaotic propagation effects [35, 36].

The paper is organized as follows. In Sec. II we introduce the Hamiltonian and general classification of quantum states for N two-level qubits strongly coupled to a quantized cavity mode, including the spread of transition frequencies and coupling strengths. In Section III we add the effects of dissipation, dephasing, and noise to the model using the stochastic equation of evolution, which we introduced in more detail elsewhere [18, 19]. In Section IV we obtain analytic solutions of the equations formulated in Sec. III and provide numerical examples illustrating dissipation-driven formation of entangled dark states decoupled from the cavity field as well as the corresponding emission spectra. In Sec. V we generalize the analysis of Sec. IV to include a large spread of transition frequencies of the qubits and band-to-band transitions in multi-level electron systems. In Section VI we further generalize the analysis of the same model to provide the classification of bright and dark states for arbitrary M-photon excitations in dissipative strongly coupled N-qubit systems and illustrate this formalism with analytic results and numerical examples for small values of M and N. Appendix A derives some useful analytic formulas for the spatial field distribution in the practically important case of a nanocavity formed by a metallic nanotip or a nanoparticle over a metallic substrate, which has been used in a variety of recent experiments. Appendix B derives approximate analytic results for quantum dynamics of inhomogeneously broadened ensembles of qubits.

Since most results in this paper are in the analytic form and the plots are normalized, here, we list typical values of the parameters in experimental solid-state nanophotonic systems which determine the strength of light-matter coupling and relaxation rates. Strong-coupling cavity QED experiments with molecular quantum emitters typically employ fluorescent organic dye molecules. The dipole moments of electronic transitions for a single molecule vary

from several D [20] to 10-20 D [37, 38]. J-aggregates of tens or hundreds of molecules were used to achieve strong and even ultrastrong coupling regime [38–40]. Molecular vibrational transitions have typical dipole moments in the $\sim 0.1-2$ D range [42]. Vibrational strong coupling in the mid-infrared has been achieved for molecular ensembles [43]. Semiconductor quantum dots (QDs) make another popular choice of a quantum emitter in strong coupling experiments. Early demonstrations of strong coupling to a single QD involved an epitaxial III-V QD with a large interband dipole moment of ~ 30 D in a dielectric microcavity at low temperature [44, 45]. More recent strong-coupling experiments with a single quantum emitter at room temperature utilized colloidal QDs [46] with lower dipole moments $\sim 5-10$ D but placed in a plasmonic nanocavity [5, 23–25, 47, 48].

The relaxation times in quantum emitters are strongly dependent on temperature, cavity geometry, and material quality. At low temperatures, the linewidth of an electronic transition in molecules in diffraction-limited microcavities reaches the natural width limited by radiative transitions, 20-40 MHz [37, 49]. For an epitaxial QD in a solid matrix the linewidth is in tens of GHz [44]. For colloidal QDs at room temperature the total linewidth reaches tens of meV [24, 25, 46]. The radiative lifetimes are from a few to a few tens of ns, both for QDs [24, 44, 46, 50] and for electronic transitions in molecules [37, 41]. Furthermore, when the qubits are placed in a plasmonic nanocavity, the decay time of their excited state is shortened due to coupling to nonradiative plasmon modes and Ohmic dissipation of the optical near field of quantum emitters in the metal [5, 50, 51], while still remaining much longer than the photon lifetime in plasmonic nanocavities which is in tens of fs [52].

Photon decay times are longest for dielectric microcavities: photonic crystal cavities, nanopillars, Fabry-Perot cavities, distributed Bragg reflector mirrors, etc. Their quality factors are typically between 10^3-10^7, corresponding to photon lifetimes from sub-ns to μs. However, the field localization in the dielectric cavities is diffraction-limited, which limits the attainable single-qubit vacuum Rabi frequency values to hundreds of μeV. Therefore, the strong coupling regime for a single or few quantum emitters is possible only at low temperatures. Interestingly, even in these experiments the cavity decay rate is faster than the decoherence of quantum emitters, although not by orders of magnitude; see, e.g., [37, 44, 45, 49]. In plasmonic nanocavites based on metallic nanoparticles, nanotips, or nanogaps, single-emitter Rabi splitting on the order of 100–300 meV has been observed [20–25], enabling room-temperature strong coupling.

II. N QUBITS IN A NONUNIFORM NANOCAVITY FIELD: THE MODEL

Our formalism is applicable to any open cavity QED system with a few or many qubits located in a nonuniform cavity field. The results are particularly important for metallic nanocavities with strong field nonuniformity on the nm scale and ultrashort photon limetimes. Therefore, we will have in mind a plasmonic nanocavity formed, e.g., by a nanotip or nanoparticle over a metallic substrate [23, 25, 51, 52] as sketched in Fig. 1a or a graphene nanostructure supporting surface plasmon-polariton modes as in Fig. 1b (e.g., [53, 54]).

We begin by introducing the Hamiltonian and defining the variables for N two-level systems with states $|0_j\rangle$ and $|1_j\rangle$, where $j=1,...N$, with energy levels 0 and W_j. We introduce the operators of annihilation and creation of an excited state, $|1_j\rangle$, $\hat{\sigma}_j=|0_j\rangle\langle 1_j|$ and $\hat{\sigma}_j^\dagger=|1_j\rangle\langle 0_j|$, which satisfy standard (anti)commutation relations within each qubit: $\hat{\sigma_j}^\dagger|0_j\rangle=|1_j\rangle$, $\hat{\sigma_j}|1_j\rangle=|0_j\rangle$, $\hat{\sigma_j}\hat{\sigma_j}=\hat{\sigma_j}^\dagger\hat{\sigma_j}^\dagger=0$; $\hat{\sigma_j}\hat{\sigma_j}^\dagger+\hat{\sigma_j}^\dagger\hat{\sigma_j}=1$. Then one can define the dipole moment operator, $\hat{\mathbf{d}}=\sum_{j=1}^{N}\left(\mathbf{d_j}\hat{\sigma}_j^\dagger+\mathbf{d_j^*}\hat{\sigma}_j\right)$, where $\mathbf{d_j}=\langle 1_j|\hat{\mathbf{d}}|0_j\rangle$, and the Hamiltonian for all qubits, $\hat{H}_a=\sum_{j=1}^{N}W_j\hat{\sigma}_j^\dagger\hat{\sigma}_j$. The N-qubit system interacts with a single-mode field $\hat{\mathbf{E}}=\mathbf{E}(\mathbf{r})\hat{c}+\mathbf{E}^*(\mathbf{r})\hat{c}^\dagger$, where $\hat{c}$ and $\hat{c}^\dagger$ are standard annihilation and creation operators for bosonic Fock states. The function $\mathbf{E}(\mathbf{r})$ is the spatial structure of the electric field in a cavity. It is normalized as in [55]

$$\int_V \frac{\partial\left[\omega^2\varepsilon\left(\omega,\mathbf{r}\right)\right]}{\omega\partial\omega}\mathbf{E}^*(\mathbf{r})\mathbf{E}(\mathbf{r})d^3r=4\pi\hbar\omega \tag{1}$$

to preserve the standard form of the field Hamiltonian, $\hat{H}_{em}=\hbar\omega\left(\hat{c}^\dagger\hat{c}+\frac{1}{2}\right)$. Here V is a quantization volume and $\varepsilon\left(\omega,\mathbf{r}\right)$ is the dielectric function of a dispersive medium that fills the cavity. The relation between the modal frequency ω and the function $\mathbf{E}(\mathbf{r})$ can be found by solving the classical electrodynamics boundary-value problem corresponding to the cavity in question.

The total Hamiltonian after adding the electric-dipole interaction with the field within the rotating wave approximation (RWA) is

$$\hat{H}=\hbar\omega\left(\hat{c}^\dagger\hat{c}+\frac{1}{2}\right)+\sum_{j=1}^{N}W_j\hat{\sigma}_j^\dagger\hat{\sigma}_j-\hbar\sum_{j=1}^{N}\left(\Omega_{Rj}\hat{\sigma}_j^\dagger\hat{c}+h.c.\right), \tag{2}$$

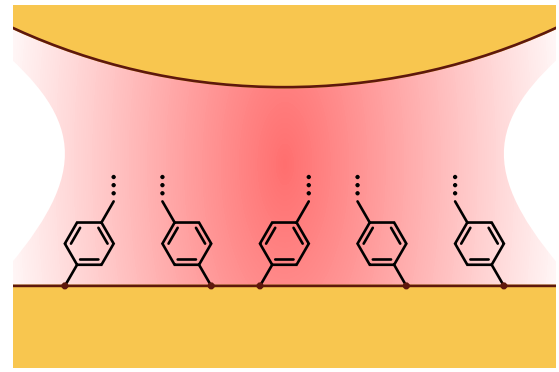

(a)

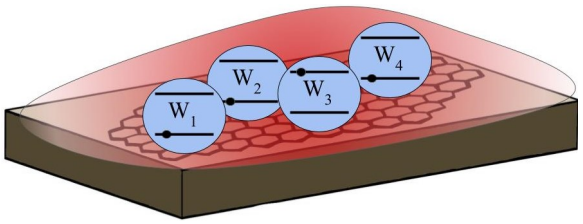

(b)

FIG. 1: An ensemble of quantum emitters (e.g. quantum dots or molecules) in a nanocavity consisting of (a) a metallic nanoparticle or nanotip of the scanning probe above a metallic substrate, or (b) a graphene nanopatch supporting a surface plasmon-polariton mode.

where $\Omega_{Rj} = \frac{\mathbf{d_j}\cdot\mathbf{E}(\mathbf{r_j})}{\hbar}$ is the Rabi frequency for the jth qubit located at the position $\mathbf{r_j}$ in the cavity. Note that this model includes a spread of the transition energies of the qubits W_j, and the variation of the cavity EM field depending on the position of each qubit, which is essential for any nanocavity. Therefore, the model loses permutation symmetry which was used to drastically simplify the analysis in [6, 7]. Nevertheless, as we show below, a significant reduction in the dimensionality of the problem is possible in our case too.

Hereafter, we will use the Hamiltonian in the interaction picture:

$$\hat{H}_{int} = -\hbar \sum_{j=1}^{N} \left(\Omega_{Rj} \hat{\sigma}_j^{\dagger} \hat{c} e^{i\Delta_j t} + h.c. \right), \tag{3}$$

where $\Delta_j = \frac{W_j}{\hbar} - \omega$. For an arbitrary quantum state of the N-qubit system coupled to a cavity mode, the state vector can be expanded over all possible combinations of subsystems as

$$\Psi = \sum_{n=0}^{\infty} \sum_{p=0}^{N} \sum_{\alpha_p=1}^{\mathcal{C}_N^p} C_{np\alpha_p} |n\rangle |p, \alpha_p\rangle, \tag{4}$$

where $|n\rangle$ is a Fock state of the boson (EM) field, $|p, \alpha_p\rangle$ is a qubit state, and $C_{np\alpha_p}$ are the complex amplitudes to be determined. Here, the index α_p denotes *different* subsets of p elements out of a set of $j = 1, 2, \ldots N$, which correspond to the excitation of p qubits out of N. The total number of such subsets is determined by the binomial coefficient

$\mathcal{C}_N^p = \frac{N!}{p!(N-p)!}$. The state $|p, \alpha_p\rangle$ can be written as

$$|p, \alpha_p\rangle = \left(\prod_{j_p \in \alpha_p} \left| \hat{\sigma}_{j_p}^\dagger \right\rangle \right) |0_{qub}\rangle,$$

where $j_p \in \alpha_p$ are qubit numbers belonging to the subset marked by index α_p and

$$|0_{qub}\rangle = \prod_{j=1}^{N} |0_j\rangle = |0, \alpha_0\rangle. \tag{5}$$

As a reminder, when the coefficients $C_{np\alpha_p}$ are calculated using the Hamiltonian (3) then the operators used to calculate the observables should be transformed in the same way the Hamiltonian (2) was transformed into the interaction picture, Eq. (3), namely $\hat{\sigma}_j \to \hat{\sigma}_j e^{-i\frac{W_j}{\hbar}t}$ and $\hat{c} \to \hat{c}e^{-i\omega t}$.

Similar to the case of identical qubits and identical field strength at the location of each qubit [6], the Schrödinger equation with the Hamiltonian (3) leads to a set of linear equations for the probability amplitudes $C_{np\alpha_p}$ which can be split into independent blocks corresponding to the condition

$$n + p = M = \text{const}. \tag{6}$$

The dimension of the Hilbert space within each independent block is $\sum_{p=0}^{\min[M,N]} \mathcal{C}_N^p$; for $M \geq N$ it is equal to $\sum_{p=0}^{N} \mathcal{C}_N^p = 2^N$. Further reduction of the dimensionality of the problem would require identical values of the W_j and Ω_{Rj} in which case all states including initial conditions have exact permutation symmetry and one could sum over all states corresponding to various combinations α_p made of p excited atoms; see [7] and the discussion in Section VI.

As we discuss in Section VI, in the presence of dissipation and noise, the noise source terms couple the groups with different values of M. However, in the strong coupling regime, such noise-induced coupling scales as a small ratio of dissipation rates to the Rabi frequency and therefore can be included perturbatively. A similar perturbative approach has been developed for nonlinear strong coupling of electron-photon-phonon systems [56]. In practice, the generation of nonclassical *multiphoton* number states is still a tremendous experimental challenge. Therefore, in Sections III-V we choose initial conditions corresponding to single-photon excitation energies. Single-photon sources of quantum light are readily available and can be used for initialization of both single- and many-qubit states with a single-photon excitation energy. These are widely used in quantum information applications, including, for example, Bell states and their generalizations to many-qubit systems; see, e.g., [57, 58]. With single-photon excitations as initial conditions, the states that can be reached as a result of evolution of the system include the ground state $|0\rangle \Pi_{j=1}^N |0_j\rangle$ and the states with energies close to the single-photon energy:

$$\Psi = C_{00} |0\rangle \Pi_{j=1}^N |0_j\rangle + C_{10} |1\rangle \Pi_{j=1}^N |0_j\rangle + \sum_{j=1}^{N} C_{0j} |0\rangle |1_j\rangle \Pi_{m\neq j}^N |0_m\rangle, \tag{7}$$

where the time-dependent complex amplitudes C_{00}, C_{10}, and C_{0j} fully characterize a given quantum state and are to be determined from the analysis below. We postpone the analysis of arbitrary multiphoton excitations with fully quantized multiphoton states until Sec. VI.

III. DESCRIPTION OF DISSIPATION AND NOISE USING STOCHASTIC EQUATIONS OF EVOLUTION

A standard way to include the effects of dissipation is based on the master equation for the density matrix $\hat{\rho}$ of the system [59],

$$\frac{d}{dt}\hat{\rho} = -\frac{i}{\hbar}\left[\hat{H}, \hat{\rho}\right] + \hat{L}(\hat{\rho}), \tag{8}$$

where $\hat{L}(\hat{\rho})$ is the relaxation operator. If there are S states in a given basis $|\alpha\rangle$, Eq. (8) corresponds to $\frac{1}{2}S(S+1)$ equations for the matrix elements $\rho_{\alpha\beta} = \rho_{\beta\alpha}^*$. The number of equations that need to be solved can be reduced to S via the method of the stochastic equation of evolution for the state vector [11–19]. This becomes possible if the structure of the relaxation operator permits representing the right-hand side of Eq. (8) in the form

$$-\frac{i}{\hbar}\left[\hat{H}, \hat{\rho}\right] + \hat{L}(\hat{\rho}) = -\frac{i}{\hbar}(\hat{H}_{eff}\hat{\rho} - \hat{\rho}\hat{H}_{eff}^\dagger) + \delta\hat{L}(\hat{\rho}), \tag{9}$$

where $\hat{H}_{eff} = \hat{H} + \hat{H}^{(ah)}$ is an effective non-Hermitian Hamiltonian.

Within the Markovian models of relaxation, the stochastic equation for the state vector takes the form

$$\frac{d}{dt}\left|\Psi\right\rangle = -\frac{i}{\hbar}\hat{H}_{eff}\left|\Psi\right\rangle - \frac{i}{\hbar}\left|\mathfrak{R}\right\rangle. \tag{10}$$

In Eq. (10) the vector $|\mathfrak{R}\rangle$ is a stochastic Langevin source with the following statistical properties:

$$\overline{\left|\mathfrak{R}\right\rangle} = 0, \quad \overline{\mathfrak{R}_\alpha\left(t'\right)\mathfrak{R}^*_\beta\left(t''\right)} = \hbar^2\delta\left(t'-t''\right)D_{\alpha\beta}, \quad D_{\alpha\beta} = \left\langle\alpha\right|\delta\hat{L}(\hat{\rho})\left|\beta\right\rangle_{\hat{\rho}\Longrightarrow\overline{\left|\Psi\right\rangle\left\langle\Psi\right|}}; \tag{11}$$

the overbar $\overline{(\cdots)}$ means averaging over the noise statistics, $\mathfrak{R}_\alpha = \langle\alpha|\,\mathfrak{R}\rangle$. The dyadics $\overline{C_\alpha C^*_\beta}$ in Eqs. (10),(11) where $C_\alpha = \langle\alpha|\,\Psi\rangle$ correspond to the density matrix elements $\rho_{\alpha\beta}$ in the master equation (see the proof in [18]).

The observables in the method of the stochastic equation are determined by $g = \overline{\langle\Psi|\,\hat{g}\,|\Psi\rangle}$, where $\hat{g}$ is an operator corresponding to the physical quantity g. This definition differs from a standard one by an additional averaging over the noise statistics. The choice of operators $\hat{H}^{(ah)}$ and correlators $D_{\alpha\beta}$ should ensure the conservation of the norm of the stochastic vector, $\overline{\langle\Psi|\,\Psi\rangle} = 1$, and bring the system to a physically reasonable steady state in the absence of external perturbation.

Another widely used method to include the effects of dissipation in quantum optics is the Heisenberg–Langevin approach [60, 61]. However, when applied to the dynamics of strongly coupled systems, the Heisenberg equations become nonlinear (see, e.g., [60]), whereas the stochastic equation for the state vector, Eq. (10), is always linear, which is an important advantage of this method.

The representation of the type shown in Eq. (9) is possible, in particular, for the Lindblad relaxation operator. Here we will use the Lindbladian $\hat{L}(\hat{\rho})$ in the case of independent dissipative reservoirs for the field and qubits and at zero temperature:

$$L(\hat{\rho}) = -\Sigma_j[\frac{\gamma_j}{2}(\hat{\sigma}_j^\dagger\hat{\sigma}_j\hat{\rho} + \hat{\rho}\hat{\sigma}_j^\dagger\hat{\sigma}_j - 2\hat{\sigma}_j\hat{\rho}\hat{\sigma}_j^\dagger)] - \frac{\mu}{2}(\hat{c}^\dagger\hat{c}\hat{\rho} + \hat{\rho}\hat{c}^\dagger\hat{c} - 2\hat{c}\hat{\rho}\hat{c}^\dagger), \tag{12}$$

which gives

$$\hat{H}_{eff} = \hat{H} - i\hbar\frac{1}{2}\left(\sum_j\gamma_j\hat{\sigma}_j^\dagger\hat{\sigma}_j + \mu\hat{c}^\dagger\hat{c}\right),\ \delta\hat{L}(\hat{\rho}) = \sum_j\gamma_j\hat{\sigma}_j\hat{\rho}\hat{\sigma}_j^\dagger + \mu\hat{c}\hat{\rho}\hat{c}^\dagger. \tag{13}$$

Here the relaxation constants μ and γ_i are determined by the cavity Q-factor and inelastic relaxation of the qubits, respectively. The Q-factor is determined by adding up diffraction and Ohmic losses in a cavity; e.g., [62, 63]. Elastic relaxation processes (pure dephasing) are included later in this section. The case of arbitrary temperatures is considered in [18]. Note that for a qubit with the transition in the visible or near-IR range, even a room-temperature reservoir is effectively at zero temperature.

Introducing state vectors Ψ of the type given in Eq. (7), we obtain a set of stochastic equations for the amplitudes,

$$\dot{C}_{00} + \gamma_{00}C_{00} = -\frac{i}{\hbar}\mathfrak{R}_{00}, \tag{14}$$

$$\dot{C}_{10} + \gamma_{10}C_{10} - i\sum_{j=1}^{N}\Omega^*_{Rj}C_{0j}e^{-i\Delta_j t} = -\frac{i}{\hbar}\mathfrak{R}_{10}, \tag{15}$$

$$\dot{C}_{0j} - \gamma_{0j}C_{0j} - i\Omega_{Rj}C_{10}e^{i\Delta_j t} = -\frac{i}{\hbar}\mathfrak{R}_{0j}, \tag{16}$$

where the relaxation constants are related to the EM field and qubit relaxation constants in the Lindbladian Eq. (12) by

$$\gamma_{00} = 0,\ \gamma_{10} = \frac{\mu}{2},\ \gamma_{0j} = \frac{\gamma_j}{2}. \tag{17}$$

The noise properties are given by

$$\overline{\mathfrak{R}^*_{\alpha n}\left(t'\right)\mathfrak{R}_{\beta m}\left(t''\right)} = \hbar^2\delta_{\alpha\beta}\delta_{nm}D_{\alpha n,\alpha n}\delta\left(t'-t''\right), \tag{18}$$

$$D_{00,00} = \sum_{j=1}^{N} \gamma_j \overline{|C_{0j}|^2} + \mu \overline{|C_{10}|^2},\ D_{10,10} = 0,\ D_{0j,0j} = 0. \tag{19}$$

To include elastic relaxation (pure dephasing) in the Lindbladian Eq. (12) we need to add the term [64]

$$L^{(el)}(\hat{\rho}) = -\Sigma_j \left[\frac{\gamma_j^{(el)}}{2} (\hat{\sigma}_{zj}\hat{\sigma}_{zj}^{\dagger}\hat{\rho} + \hat{\rho}\hat{\sigma}_{zj}\hat{\sigma}_{zj}^{\dagger} - 2\hat{\sigma}_{zj}^{\dagger}\hat{\rho}\hat{\sigma}_{zj}) \right],$$

where $\hat{\sigma}_{zj} = \hat{\sigma}_{zj}^{\dagger} = |1_j\rangle\langle 1_j| - |0_j\rangle\langle 0_j|$ and $\gamma_j^{(el)}$ is an elastic relaxation constant. Recent analysis [18, 19] shows that for two-level qubits the elastic processes can be included by making the following replacements in the expressions for γ_{0j} and $D_{0j,0j}$: $\gamma_{0j} \Longrightarrow \gamma_{0j} + \gamma_j^{(el)}$, $D_{0j,0j} \Longrightarrow D_{0j,0j} + 2\gamma_j^{(el)}\overline{|C_{0j}|^2}$. These relationships lead to standard relaxation timescales of populations $T_{1j} = \frac{1}{\gamma_j}$ and coherence $T_{2j} = \frac{1}{\frac{1}{2T_{1j}} + \gamma_j^{(el)}}$ [64]. Therefore, including pure dephasing processes leads to corrections in the last of Eqs. (17) and the last of Eqs. (19), namely

$$\gamma_{0j} = \frac{\gamma_j}{2} + \gamma_j^{(el)},\ D_{0j,0j} = 2\gamma_j^{(el)}\overline{|C_{0j}|^2}. \tag{20}$$

Taking into account Eqs. (20), it is easy to show that for any set of elastic scattering rates Eqs. (14)-(16) conserve the norm:

$$\sum_{j=1}^{N} \overline{|C_{0j}|^2} + \overline{|C_{10}|^2} + \overline{|C_{00}|^2} = 1; \tag{21}$$

and Eqs. (15)-(16) preserve the following relationship which includes only the rates of *inelastic* relaxation:

$$\frac{d}{dt}\left(\sum_{j=1}^{N} \overline{|C_{0j}|^2} + \overline{|C_{10}|^2} \right) = -\sum_{j=1}^{N} \gamma_j \overline{|C_{0j}|^2} - \mu \overline{|C_{10}|^2}. \tag{22}$$

If pure dephasing processes can be neglected and the reservoir temperature is much lower than the optical transition frequency (in energy units), we always have $D_{0j,0j} = D_{10,10} = 0$, which, together with $\overline{\mathfrak{R}_{10}} = \overline{\mathfrak{R}_{0j}} = 0$, allows one to neglect the contribution of noise sources $\mathfrak{R}_{10}$ and $\mathfrak{R}_{0j}$ when calculating observables; see [18, 19]. In this case, Eqs. (14)-(16) can be considered an improved version of the Weisskopf-Wigner approximation, because they not only include dissipation as imaginary parts of eigenenergies but also conserve the norm of the state vector; see Eq. (21).

IV. QUANTUM DYNAMICS AND EMISSION SPECTRUM OF AN ENSEMBLE OF QUBITS WITH EQUAL TRANSITION FREQUENCIES

A. Analytic solution for quantum dynamics in a nonuniform cavity field

Here we consider a low-Q plasmonic cavity with a field decay time much shorter than dissipation times in qubits $T_{(1,2)j}$. In this case the dissipation is dominated by the field decay, and we can put $\gamma_{0j} \approx 0$ in Eqs. (14)-(16). Furthermore, considering the low-temperature limit (as compared to the optical frequency) we can put $\gamma_{00} = D_{0j,0j} = D_{10,10} = 0$, which, together with $\overline{\mathfrak{R}_{10}} = \overline{\mathfrak{R}_{0j}} = 0$, allows one to neglect the effect of noise terms $\mathfrak{R}_{10}$ and $\mathfrak{R}_{0j}$ [18, 19]. Of course the resulting solutions will be valid at the intermediate timescales shorter than the qubit relaxation times. The solution including qubit relaxation is equally straightforward to obtain, but it is more cumbersome.

The resulting coupled equations for the probability amplitudes C_{10} and C_{0j} read

$$\dot{C}_{10} + \frac{\mu}{2} C_{10} - i \sum_{j=1}^{N} \Omega_{Rj}^{*} C_{0j} e^{-i\Delta_j t} = 0, \tag{23}$$

$$\dot{C}_{0j} - i\Omega_{Rj} C_{10} e^{i\Delta_j t} = 0, \tag{24}$$

whereas the solution for the amplitude of the ground state is

$$C_{00}(t) = C_{00}(t=0) - \frac{i}{\hbar}\int_0^t \mathfrak{R}_{00} dt, \tag{25}$$

so that $\overline{C_{00}(t) - C_{00}(t=0)} = 0$. The value of $\overline{C_{00}^2(t)}$ can be also determined directly from the conservation law (21), but we will need Eq. (25) when calculating the emission spectrum below.

These equations can be immediately solved for an ensemble of qubits with the same transition frequencies but with different Rabi frequencies since they are located in a nonuniform field of a nanocavity. The case of different transition frequencies is considered in the next section. We can put $\Delta_j = 0$ in Eqs. (23), (24) and introduce the new variable

$$F = \sum_{j=1}^{N} \Omega_{Rj}^* C_{0j}, \tag{26}$$

which yields

$$\dot{C}_{10} + \frac{\mu}{2} C_{10} - iF = 0, \tag{27}$$

$$\dot{F} - i\Omega_N^2 C_{10} = 0, \tag{28}$$

where

$$\Omega_N^2 = \sum_{j=1}^{N} |\Omega_{Rj}|^2 \tag{29}$$

is a collective Rabi frequency. The initial conditions $C_{10}(0) = F(0) = 0$ give a trivial steady state solution, and there is an infinite number of states corresponding to $F = 0$.

Seeking the solution $\propto e^{\Gamma t}$ gives

$$\begin{pmatrix} C_{10} \\ F \end{pmatrix} = e^{-\frac{\mu}{4}t} \left[A e^{i\Sigma t} \begin{pmatrix} 1 \\ K_1 \end{pmatrix} + B e^{-i\Sigma t} \begin{pmatrix} 1 \\ K_2 \end{pmatrix} \right], \tag{30}$$

where

$$K_{1,2} = \pm\Sigma - i\frac{\mu}{4},\ \Sigma = \sqrt{\Omega_N^2 - \frac{\mu^2}{16}} \tag{31}$$

and the constants A and B are given by the initial conditions

$$A = \frac{K_2 C_{10}(0) - F(0)}{K_2 - K_1},\ B = \frac{F(0) - K_1 C_{10}(0)}{K_2 - K_1},$$

and

$$F(0) = \sum_{j=1}^{N} \Omega_{Rj}^* C_{0j}(0).$$

Similarly, from Eq. (24) when $\Delta_j = 0$ we obtain

$$C_{0j}(t) = C_{0j}(0) + i\Omega_{Rj} \int_0^t C_{10}(t')dt'. \tag{32}$$

Using the solution for C_{10} which follows from Eq. (30),

$$C_{10}(t) = \left[C_{10}(0) \left(\cos\Sigma t - \frac{\mu}{4\Sigma} \sin\Sigma t \right) + i\frac{F(0)}{\Sigma} \sin\Sigma t \right] e^{-\frac{\mu}{4}t}, \tag{33}$$

we arrive at

$$C_{0j}(\infty) = C_{0j}(0) - \Omega_{Rj} \frac{F(0)}{\Omega_N^2}. \tag{34}$$

Note that Eq. (34) is valid for any μ.

At long times one always has $C_{10}(\infty) = F(\infty) = 0$. Therefore, for the initial state satisfying the condition

$$\frac{C_{0j}(0)}{C_{0i}(0)} = \frac{\Omega_{Rj}}{\Omega_{Ri}}, \tag{35}$$

all energy stored initially in the qubit system is radiated away over a short cavity decay time $\sim 1/\mu$. Such a state is the generalization of the bright Dicke state (see, e.g., [7, 58]) to an ensemble of quantum emitters strongly coupled to a spatially nonuniform field of a plasmonic cavity.

Consider an arbitrary initial state:

$$|\Psi(0)\rangle = \begin{pmatrix} C_{00}(0) \\ C_{10}(0) \\ C_{01}(0) \\ ... \\ C_{0j}(0) \\ ... \\ C_{0N}(0) \end{pmatrix} = \begin{pmatrix} C_{00}(0) \\ 0 \\ 0 \\ ... \\ 0 \\ ... \\ 0 \end{pmatrix} + \begin{pmatrix} 0 \\ C_{10}(0) \\ C_{01}(0) \\ ... \\ C_{0j}(0) \\ ... \\ C_{0N}(0) \end{pmatrix}. \tag{36}$$

We are interested in the subset of equations for variables C_{10} and C_{0j} that end up being separated from the ground state. Since the system is linear, we can split the last column on the right-hand side of Eq. (36) into two components:

$$\begin{pmatrix} C_{10}(0) \\ C_{01}(0) \\ ... \\ C_{0j}(0) \\ ... \\ C_{0N}(0) \end{pmatrix} = \begin{pmatrix} 0 \\ C_{01}(0) - \Omega_{R1}\frac{F(0)}{\Omega_N^2} \\ ... \\ C_{0j}(0) - \Omega_{Rj}\frac{F(0)}{\Omega_N^2} \\ ... \\ C_{0N}(0) - \Omega_{RN}\frac{F(0)}{\Omega_N^2} \end{pmatrix} + \begin{pmatrix} C_{10}(0) \\ \Omega_{R1}\frac{F(0)}{\Omega_N^2} \\ ... \\ \Omega_{Rj}\frac{F(0)}{\Omega_N^2} \\ ... \\ \Omega_{RN}\frac{F(0)}{\Omega_N^2} \end{pmatrix}. \tag{37}$$

It is easy to see that the first column on the right-hand side of Eq. (37) corresponds to a stationary (dark) state with $C_{10} = F = 0$. The second column gives rise to the bright state found before. As a result, we obtain

$$C_{10}(\infty) = 0,\ C_{0j}(\infty) = C_{0j}(0) - \Omega_{Rj}\frac{\sum_{m=1}^{N}\Omega_{Rm}^* C_{0m}(0)}{\sum_{j=1}^{N}|\Omega_{Rj}|^2}. \tag{38}$$

Then from Eq. (21) the amplitude of the ground state is given by

$$|C_{00}(\infty)|^2 = 1 - \sum_{j=1}^{N}\left|C_{0j}(0) - \Omega_{Rj}\frac{\sum_{m=1}^{N}\Omega_{Rm}^* C_{0m}(0)}{\sum_{j=1}^{N}|\Omega_{Rj}|^2}\right|^2. \tag{39}$$

It is clear from Eqs. (38) and (39) that if the number J of initially excited qubits is much smaller than the total number of qubits, $J \ll N$, then the change of the initial quantum state of the qubit ensemble is of the order of J/N. Therefore, an ensemble of ground-state qubits effectively shields an arbitrary initial state of a relatively small group of excited qubits from coupling to the cavity field. The shielding is due to formation of an entangled dark state in which the destructive interference leads to decoupling of the many-body state from the cavity field, even though each qubit remains strongly coupled to the quantum field of a cavity.

The following numerical example in Fig. 2 illustrates the formation of an entangled dark state in an ensemble of qubits in a nonuniform field of a nanocavity. To have an explicit analytic expression for the nanocavity field distribution we use the model described in Appendix A: a metallic sphere over a metallic substrate, where the metallic sphere can represent a nanoparticle or an apex of a nanotip as in recent strong-coupling experiments [20, 22, 23, 25, 48]. For a strongly subwavelength field localization the quasielectrostatic approximation is valid and one can solve the electrostatic boundary-value problem for a given geometry. As we discuss in Appendix A, this restricts the spectral range to near-infrared or longer wavelengths, in order to stay away from the interband transition region and plasmon resonances. Rigorous modeling of plasmonic nanocavities is outside the scope of this paper; we just need an example of a spatial field distribution. There is an extensive literature on theoretical and numerical approaches to describe lossy and leaky plasmonic cavity modes; see, e.g. a recent review [52] or [65]. For our example, we take the sphere of radius $R = 10$ nm with its center located on z-axis at $z_0 = 1.2R$ above the substrate. We will use the line charge approximation (A21) for the electric field of a cavity mode, which is an excellent approximation to the exact formula,

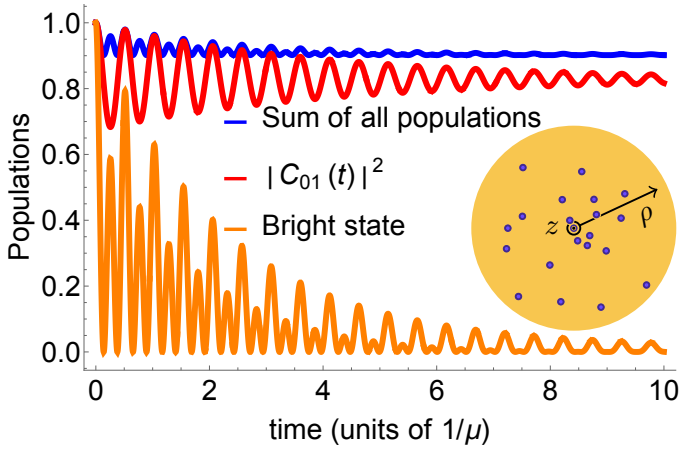

FIG. 2: Time evolution of the populations for an ensemble of $N = 21$ qubits in the nanocavity formed by the metallic sphere of radius $R = 10$ nm with its center located on z-axis at $z_0 = 12$ nm above the substrate; see Appendix A for the field distribution. The molecules are assumed to be distributed uniformly within a circle of radius 10 nm on the substrate, with the center of the circle at the cavity axis $\rho = 0$. The inset shows the top view of one possible realization of this distribution, with random angular positions in the substrate plane. The effective cavity volume is 50 nm^3, the transition dipole moment is 10 Debye, the Rabi frequency at $\rho = 0$ is 120 meV, and the cavity decay time is $1/\mu = 20$ fs. Top blue curve: The sum of the occupation probabilities of all qubits $\sum_{j=1}^{N} |C_{0j}|^2$ when only the qubit in the center of the cavity is excited, i.e., $C_{01}(0) = 1$; middle red curve: the occupation $|C_{01}(t)|^2$ of the initially excited qubit; bottom orange curve: the sum of all occupation probabilities when the qubits were initally prepared in the bright state (35).

as one can see from the middle plot in Fig. 12. Let us take $N = 21$ qubits distributed uniformly on the substrate at distances from $\rho = 0$ to 10 nm from the z-axis. The inset shows the top view of one possible realization of this distribution. The angular positions of the qubits in the substrate plane are randomly generated and do not affect the results, because the cavity field has an axial symmetry. As a reminder, we neglect any direct coupling between the qubits due to, e.g., their dipole-dipole interactions.

First we consider an arbitrary initial state which is neither bright nor dark. Let us assume for definiteness that only one qubit located at the maximum field $\rho = 0$ is initially excited, i.e., its initial probability amplitude $C_{01}(t = 0) = 1$, whereas all other qubits are in the ground state. The subsequent excitation of this qubit as described by $|C_{01}(t)|^2$ is shown as the middle red curve in Fig. 2, whereas the sum of populations of all qubits is the top blue curve. As is obvious from the picture, after the bright state component of the initial state is radiated away over a short time of a few $1/\mu$, the system remains in an entangled dark state which is decoupled from the cavity mode and has a lifetime determined by relaxation constants of the qubits. This can also be verified by calculating $F(t)$ from Eq. (26) which approaches zero over the same timescale. Only a few per cent ($\sim 1/N$) of the total excitation energy is radiated away. This result remains qualitatively the same when we vary the distribution of the initial excitation; only the fraction of the radiated energy changes. The dynamics changes if the system was initially prepared *exactly* in the bright state described by Eq. (35). In this case *all* initial excitation is radiated away over the time of the order of a few $1/\mu$. The bottom (orange) curve in Fig. 2 shows the behavior of the sum of all qubit populations when the system starts from the bright state.

If the cavity size is increased by, e.g., increasing the value of R, the collective Rabi frequency Ω_N decreases as $V^{-1/2}$, where V is the cavity volume. According to in Eqs. (30) and (31), this will increase the period of oscillations of populations in Fig. 2, but the fraction of the excitation energy left in the dark state will remain the same. Moreover, the dark state will survive even if Ω_N becomes smaller than the cavity decay rate $\mu/4$, as long as Ω_N remains greater than $\sqrt{\gamma_{0j}\mu}/2$, where γ_{0j} is the relaxation rate for the qubits defined in the previous section and assumed to be the same for all qubits here. However, this robustness of the dark state only exists for identical qubits. As we will see in Sec. V, for an ensemble of qubits with a large spread of transition frequencies Δ_m, the reduction of the collective Rabi frequency below Δ_m destroys the dark state. Furthermore, as we discuss in Sec. VI, for multiphoton excitations reducing the collective Rabi frequency below the cavity decay rate activates noise terms which couple eigenstates with different excitation energies and effectively accelerate the relaxation in the qubit ensemble. Therefore, the strong coupling condition in which Ω_N is larger than all relaxation rates in the system is essential for the dark state formation in most cases.

B. The emission spectrum

Detecting the radiation from quantum emitters placed in nanocavities is one of the most straightforward ways to study their quantum dynamics [2, 20, 23, 25, 60, 66]. The power spectrum received by the detector can be calculated as [60, 66]

$$P(\nu) = A \cdot S(\nu)$$

where

$$S(\nu) = \frac{1}{\pi}\mathrm{Re}\int_0^\infty d\tau e^{i\nu\tau}\int_0^\infty dt K(t,\tau), \tag{40}$$

$$K = \langle\Psi(0)|\,\hat{c}^\dagger(t)\,\hat{c}(t+\tau)\,|\Psi(0)\rangle; \tag{41}$$

$\hat{c}^\dagger(t)$ and $\hat{c}(t)$ are Heisenberg creation and annihilation operators for the cavity field, $\Psi(0)$ is an initial state of the system. The coefficient A is determined by the cavity design, spatial structure of the cavity field, and detector properties.

These equations indicate that to calculate the power spectrum one has to solve the Heisenberg-Langevin equations for the operators $\hat{c}(t)$ and $\hat{c}^\dagger(t)$ [60] and evaluate the correlator including averaging over the noise statistics, $K \Rightarrow \overline{\langle\Psi(0)|\,\hat{c}^\dagger(t)\,\hat{c}(t+\tau)\,|\Psi(0)\rangle}$. However, the Heisenberg-Langevin equations are nonlinear in the strong-coupling Rabi oscillations regime for a single-photon field. Therefore, it is more convenient to utilize the solution of the linear stochastic equation (10) for the state vector. The corresponding procedure is described in [56] where we prove that the correlator $K(t,\tau)$ can be calculated as

$$K(t,\tau) = \overline{\langle\,\Phi(t,\tau)\,|\Psi_C(t+\tau)\rangle}. \tag{42}$$

Here $\Psi_C(t+\tau) = \hat{c}\Psi(t+\tau)$, where $\Psi(t+\tau)$ is the solution to the stochastic Schrödinger equation (10) on the time interval $[0, t+\tau]$ with initial condition $|\Psi(0)\rangle$; $\Phi(t,\tau)$ is the solution to Eq. (10) on the time interval $[t, t+\tau]$ with initial condition $\Psi_C(t)$, and $\Psi_C(t) = \hat{c}\Psi(t)$, where $\Psi(t)$ is also the solution Eq. (10) but over the time interval $[0,t]$. The overbar in Eq. (42) denotes averaging over the statistics of noise sources, which according to the Langevin approach is equivalent to averaging over the reservoir degrees of freedom [67].

Now we apply this formalism to calculate the emission spectrum of an excited qubit in an ensemble of ground-state qubits. Since we just want to illustrate how the formation of an entangled dark state suppresses the emission from the cavity, we can simplify algebra and consider identical Rabi frequencies: $\Omega_{Rj} = \Omega_R$, $\Omega_N^2 = N\Omega_R^2$. If needed, a more cumbersome analytic solution for the spectrum can also be readily obtained for an arbitrary distribution of Rabi frequencies using the state vector derived in the previous subsection.

As before, we will solve for the evolution over the intermediate timescales when only the field dissipation has to be taken into account. Consider an initial state in which only one qubit is excited, $|\Psi(0)\rangle = |0\rangle\,|1_1\rangle\,\Pi_{m=2}^N\,|0_m\rangle$.

As usual, we seek the solution of the stochastic equation for the state vector in the form of Eq. (7). From Eqs. (7) and (10) one can get

$$\Psi_C(t) = \hat{c}\Psi(t) = C_{10}(t)\,|0\rangle\,\Pi_{j=1}^N\,|0_j\rangle \tag{43}$$

According to the above procedure, we need to find the solution of Eqs. (23)-(25) with initial condition (43) at the time interval $[t, t+\tau]$. One can see that Eqs. (23),(24) have a trivial zero solution, whereas Eq. (25) yields

$$\Phi(t,\tau) = \left[C_{10}(t) - \frac{i}{\hbar}e^{-i\frac{\omega}{2}\tau}\int_0^\tau \mathfrak{R}_{00}(t+t')\,dt'\right]|0\rangle\,\Pi_{j=1}^N\,|0_j\rangle. \tag{44}$$

Substituting Eqs. (43) and (44) into Eq. (42) and taking into account that the term linear with respect to the noise source gives zero upon averaging, we obtain

$$K(t,\tau) = C_{10}^*(t)\,C_{10}(t+\tau). \tag{45}$$

Using Eq. (30) for the function $C_{10}(t)$ we get

$$K(t,\tau) = \frac{|\Omega_R|^2}{\Sigma^2}e^{-\frac{\mu}{4}\tau}e^{-\frac{\mu}{2}t}\sin(\Sigma t)\sin[\Sigma(t+\tau)]. \tag{46}$$

The resulting power spectrum in Eq. (40) is given by

$$S(\nu) = \frac{8\left|\Omega_R\right|^2}{\pi\mu\left(\mu^2+16\Sigma^2\right)}\mathrm{Re}\frac{\mu-2i\nu}{\left(\frac{\mu}{4}-i\nu\right)^2+\Sigma^2}.$$

Taking into account the fact that we solved the problem in the interaction picture, the measured spectrum is obtained by replacing $\nu \Rightarrow \nu-\omega$. Using also Eq. (31), we obtain

$$S(\nu) = \frac{1}{2\pi}\frac{\left|\Omega_R\right|^2}{\left((\nu-\omega)^2-\left(N\left|\Omega_R\right|^2-\frac{\mu^2}{8}\right)\right)^2+\frac{\mu^2}{4}\left(N\left|\Omega_R\right|^2-\frac{\mu^2}{16}\right)}. \tag{47}$$

Under the condition $\mu \ll 2\left|\Omega_R\right|\sqrt{N}$ the spectrum is simplified:

$$S(\nu) = \frac{1}{2\pi}\frac{\left|\Omega_R\right|^2}{\left((\nu-\omega)^2-N\left|\Omega_R\right|^2\right)^2+\frac{\mu^2}{4}N\left|\Omega_R\right|^2},$$

i.e., the spectrum consists of two well-resolved lines shifted with respect to ω by $\pm\left|\Omega_R\right|\sqrt{N}$, with the maximum value $S_{\max}\left(\pm\left|\Omega_R\right|\sqrt{N}\right) = \frac{1}{\pi}\frac{2}{N\mu^2}$ and linewidth $\sim \frac{\mu}{2}$. The dependence $S_{\max} \propto \frac{1}{N}$ reflects the destructive interference effect described above: the probability of the photon emission by a qubit scales as $P_{rad} \approx \frac{1}{N}$.

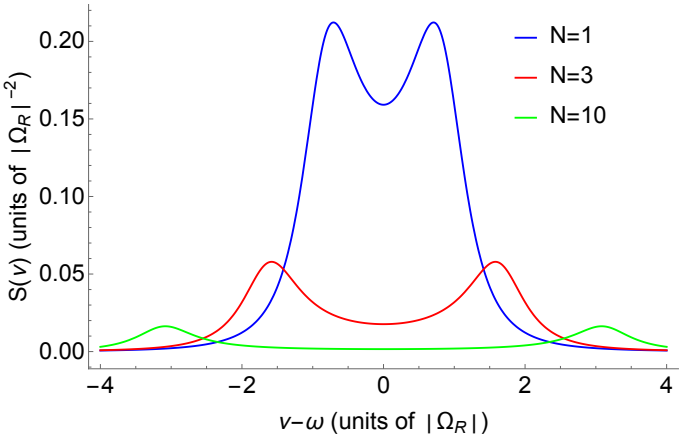

FIG. 3: Normalized emission spectra given by Eq. (47) for three values of N and the cavity decay rate $\mu/2 = \Omega_R$. The height of the peaks scales as $1/N$.

This behavior is illustrated in Fig. 3 which shows the emission spectra given by Eq. (47) for three different qubit numbers N and the cavity decay rate $\mu/2 = \Omega_R$. The most interesting result here is not the splitting of the spectrum which is an obvious consequence of strong coupling, but the fact that the peak intensity (the height of the peaks) gets suppressed with increasing N as $1/N$. This behavior is robust and does not depend on the details of initial excitation as long as the number of initially excited qubits is much smaller than N; see the discussion after Eqs. (38) and (39).

As we already pointed out, the dissipation-driven transition of a system into a dark state is not surprising by itself and has been studied before for various systems; see, e.g., the formation of subradiant states in the Dicke superradiance problem [34] or quantum dots in a plasmonic cavity [9, 10]. It is nontrivial, however, that in our case of a strongly coupled N-qubit system, the amount of energy loss from the system before it goes into the dark state approaches zero as $1/N$ due to destructive interference from unexcited qubits. It is also convenient that we have a complete analytic solution describing the effect.

V. MANY-QUBIT SYSTEMS WITH DIFFERENT TRANSITION FREQUENCIES

In this section we consider an ensemble of qubits with a large spread of transition frequencies interacting with a spatially nonuniform cavity mode. This is usually the case for quantum dots where the inhomogeneous broadening is

related to the dispersion of the dot sizes. We will assume that the inhomogeneous broadening dominates:

$$\frac{\mu}{4\Delta_m} \ll 1, \tag{48}$$

where Δ_m is the half-width of the inhomogeneous broadening. We will show below that under strong-coupling conditions the inhomogeneous broadening leads to long-period pulsations of individual qubit populations but does not prevent the formation of a collective dark state decoupled from the cavity mode, as long as the collective Rabi frequency Ω_N in Eq. (29) remains larger than Δ_m.

It follows from Eq. (24) that

$$C_{0j} = C_{0j}(0) + i\Omega_{Rj}\int_0^t C_{10}(\tau)e^{i\Delta_j\tau}d\tau, \tag{49}$$

which can be substituted into Eq. (23) to obtain

$$\dot{C}_{10} + \frac{\mu}{2}C_{10} = i\sum_{j=1}^{N}\Omega_{Rj}^* C_{0j}(0)e^{-i\Delta_j t} - \int_0^t \sum_{j=1}^{N}|\Omega_{Rj}|^2 C_{10}(\tau)e^{i\Delta_j(\tau-t)}d\tau. \tag{50}$$

Now we introduce the Laplace transform,

$$C_p = \int_0^\infty C_{10}(t)e^{-pt}dt,\ C_{10}(t) = \frac{1}{2\pi i}\int_{x-i\infty}^{x+i\infty} C_p e^{pt}dp.$$

Since the functions $\sum_{j=1}^N \Omega_{Rj}^* C_{0j}(0)e^{-i\Delta_j t}$ and $\sum_{j=1}^N |\Omega_{Rj}|^2 e^{-i\Delta_j t}$ do not grow as $t\to\infty$, we can assume $\mathrm{Re}[p] > 0$ and therefore $x > 0$. Laplace transforming Eq. (50) gives

$$pC_p - C_{10}(0) + \frac{\mu}{2}C_p = iF_p - C_p D_p, \tag{51}$$

where

$$F_p = \int_0^\infty \left(\sum_{j=1}^{N}\Omega_{Rj}^* C_{0j}(0)e^{-(i\Delta_j+p)t}\right)dt = \sum_{j=1}^{N}\frac{\Omega_{Rj}^* C_{0j}(0)}{i\Delta_j + p},$$

$$D_p = \int_0^\infty \sum_{j=1}^{N}|\Omega_{Rj}|^2 e^{-(i\Delta_j+p)t}dt = \sum_{j=1}^{N}\frac{|\Omega_{Rj}|^2}{i\Delta_j + p}.$$

Solving Eq. (51) gives

$$C_{10}(t) = \frac{1}{2\pi i}\int_{x-i\infty}^{x+i\infty}\frac{C_{10}(0) + \sum_{j=1}^N \frac{\Omega_{Rj}^* C_{0j}(0)}{i\Delta_j+p}}{p + \frac{\mu}{2} + \sum_{j=1}^N \frac{|\Omega_{Rj}|^2}{i\Delta_j+p}}e^{pt}dp. \tag{52}$$

The functions $C_{0j}(t)$ are determined by substituting Eq. (52) into Eq. (49).

The behavior of the function $C_{10}(t)$ is determined by zeros of the denominator of the integrand in Eq. (52):

$$C_{10}(t) \to \sum_k A_k e^{p_{0k}t},$$

where p_{0k} are the solutions of equation

$$\left(p + \frac{\mu}{2}\right)\Pi_j^N(i\Delta_j + p) + \sum_{j=1}^{N}|\Omega_{Rj}|^2\Pi_{k\neq j}^N(i\Delta_k + p) = 0. \tag{53}$$

Equation (53) determines a set of $N+1$ normal modes for the system of Eqs. (23) and (24) after the replacement $C_{0j}(t)e^{-i\Delta_j t} \to C_{0j}(t)$ which eliminates explicit time dependence. The Laplace transform is especially convenient in the limit of a continuous spectrum, see Appendix B. The dynamics of the populations of individual qubits should

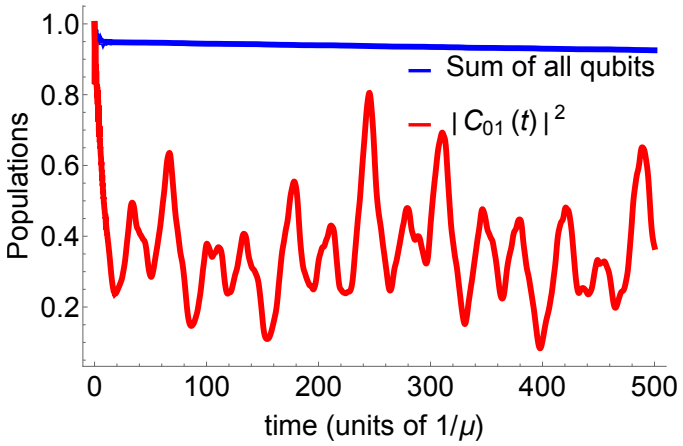

FIG. 4: Time evolution of the populations for an ensemble of $N = 41$ qubits with transition frequencies distributed pseudo-randomly in the range $\pm\Delta_m = 50$ meV around resonance with a cavity mode. The cavity decay, Rabi frequency distribution, geometry, and spatial distribution are the same as for the example in Fig. 2. Top blue curve: the sum of the occupation probabilities of all qubits $\sum_{j=1}^{N} |C_{0j}|^2$ when only one qubit in the center of the cavity is excited initially, i.e., $C_{01}(0) = 1$; bottom red curve: the occupation $|C_{01}(t)|^2$ of the initially excited qubit.

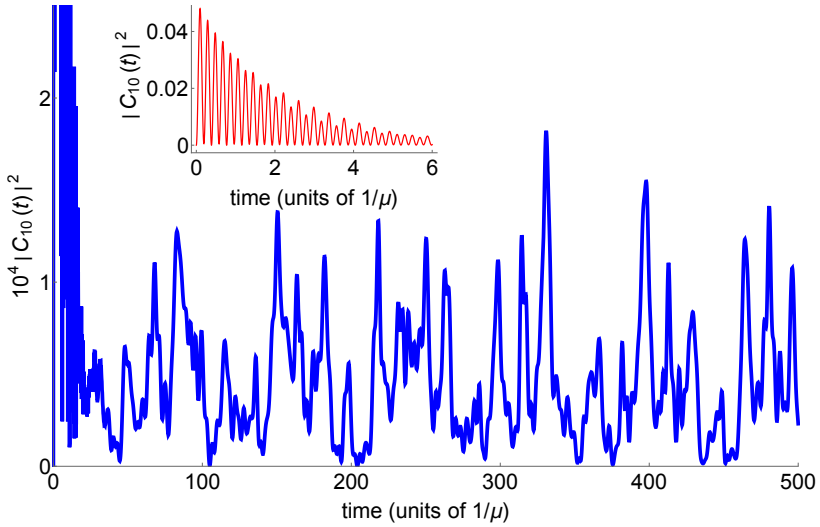

FIG. 5: Excitation probability of the cavity mode, $|C_{10}(t)|^2$, for the same conditions as in Fig. 4. Inset: same for a short initial time interval, showing initial relaxation of the cavity field and Rabi oscillations.

include the beatnotes with characteristic periods $T \sim \frac{\pi N}{\Delta_m}$. At the same time, as long as the collective Rabi frequency Ω_N remains greater than the inhomogeneous linewidth, strong coupling still leads to the formation of a collective dark state in which only a small fraction $\sim 1/N$ of the initial excitation energy is radiated away whereas the sum of all qubit populations remains approximately constant and close to its initial value.

We illustrate this dynamics by solving numerically the set of Eqs. (23) and (24) for particular values of the parameters. One example is shown in Figs. 4 and 5. Here we consider $N = 41$ qubits with transition frequencies distributed pseudo-randomly in the range $\pm\Delta_m = 50$ meV around resonance with a cavity mode, which corresponds to typical spread of frequencies of semiconductor quantum dots. The geometry and spatial distribution are the same as for the example in Fig. 2. The cavity decay time is again 20 fs, i.e., $\mu = 33$ meV and the Rabi frequency in the center of the cavity is 120 meV. As is clear from the figures, over a very short initial time of the order of several $1/\mu$ a small $\sim 1/N$ fraction of the initial excitation energy is radiated away and the entangled dark state is established. After that, individual qubit populations undergo slow quasi-chaotic oscillations, as expected from a system of coupled oscillators with incommensurate frequencies, whereas the sum of all populations remains almost constant except for a very slow decay with characteristic timescale of $> 10^4\ 1/\mu$. This decay is due to a small residual coupling to a cavity mode: as one can see from the long-time dynamics in Fig. 5, the cavity mode maintains quasi-chaotic oscillations at a very low

level of $\sim 10^{-4}$. Eventually, the relaxation of individual qubits which we neglected here will kick in, typically over ps timescales at room temperatures and ns to μs scale at low temperatures.

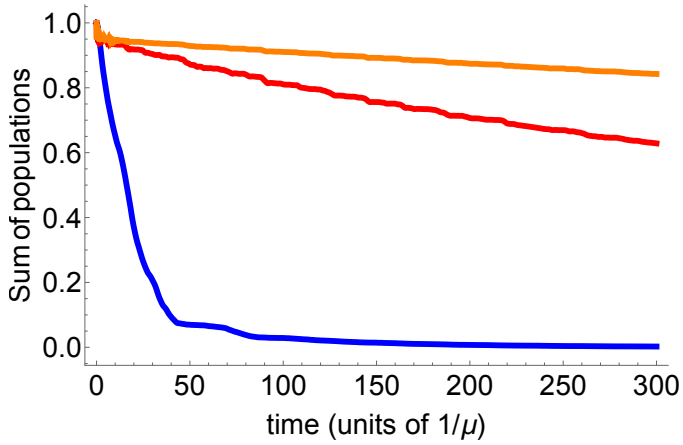

FIG. 6: Time evolution of the sum of the occupation probabilities of $N = 41$ qubits $\sum_{j=1}^{N} |C_{0j}|^2$ with transition frequencies distributed pseudo-randomly in the range $\pm\Delta_m = 90$ meV around resonance with a cavity mode. The cavity decay time, Rabi frequency distribution, geometry, and spatial distribution are the same as for the example in Fig. 2. Only one qubit in the center of the cavity is initially excited, i.e., $C_{01}(0) = 1$. Three curves correspond to three different collective Rabi frequencies Ω_N. Top orange curve: $\Omega_N = 540$ meV, middle red curve: $\Omega_N = 270$ meV, bottom blue curve: $\Omega_N = 27$ meV.

The initial stage of relaxation to the dark state ($\mu t \leq 20$) is modulated by fast Rabi oscillations that are not even visible in Fig. 4 but can be seen in the inset of Fig. 5. The subsequent slow beatnote oscillations of individual qubit populations vary from qubit to qubit and between different random realizations of the distribution of transition frequencies, but the qualitative picture remains the same. The beatnote oscillations become strictly periodic when the transition frequencies are separated by the same frequency interval, but this would be an unrealistic situation.

If the collective Rabi frequency Ω_N becomes smaller than Δ_m, for example because of an increase in the cavity volume, the decay of the sum of the occupation probabilities of all qubits $\sum_{j=1}^{N} |C_{0j}|^2$ accelerates. This is illustrated in Fig. 6 which shows the evolution of the sum of populations for three values of the Rabi frequency at the cavity center: $\Omega_R(0) = 120$ meV (top curve), 60 meV (middle curve), and 6 meV (bottom curve, which correspond the the values of the collective Rabi frequency $\Omega_N = 540$ meV, 270 meV, and 27 meV, respectively. There is an obvious shortening of the decay time when Ω_N becomes much smaller than the total spread of transition frequencies determined by $2\Delta_m = 180$ meV. With increasing spectral density of qubits the periods of beatnotes increase, eventually leading to a continuous spectrum of inhomogeneous broadening, where further analytic insights can be obtained, especially for the photon mode dynamics which is not significantly affected by beatnote oscillations. Some limiting cases are described in Appendix B.

A. Multilevel electron systems

Here we consider a multilevel quantum-confined electron system such as electron states in a quantum well or a transition-metal-dichalcogenide (TMD) monolayer, or perhaps in a quantum wire or a multilevel quantum dot. Note that quantum well structures are usually placed in planar cavities where only one dimension is subwavelength. Furthermore, all epitaxially grown semiconductor nanostructures cannot be squeezed into a nanometer gap and have to be integrated into a larger-size cavity, for example a dielectric microcavity [2, 44, 45, 68–72]. At the same time, plasmonic nanostructures and tip-induced nanocavities have been increasingly used to achieve a strong-coupling regime, especially with TMD monolayer semiconductors [73–75].

Optical transitions in such systems occur generally between two groups of electron energy states, for example between electron states in the conduction band and valence band. Let us take zero energy in the middle between these two groups and denote positive energies in the conduction band as W_j (Latin indices) and negative energies in the valence band as $-W_\alpha$ (Greek indices). The frequencies of the optical transitions are

$$\omega_{j\alpha} = \frac{W_j + W_\alpha}{\hbar}. \tag{54}$$

We do not consider here the intraband optical transitions within each group, e.g. $\alpha \iff \beta$ or $m \iff n$, although the formalism below can be easily extended to include them.

The RWA Hamiltonian is

$$\hat{H} = \hbar\omega\left(\hat{c}^{\dagger}\hat{c} + \frac{1}{2}\right) + \sum_{j=1}^{J} W_j \hat{a}_j^{\dagger}\hat{a}_j - \sum_{\alpha=1}^{A} W_\alpha \hat{a}_\alpha^{\dagger}\hat{a}_\alpha - \hbar\sum_{j=1}^{J}\sum_{\alpha=1}^{A}\left[\left(\Omega_{R;j\alpha}\hat{a}_j^{\dagger}\hat{a}_\alpha\hat{c} + \Omega_{R;j\alpha}^{*}\hat{a}_\alpha^{\dagger}\hat{a}_j\hat{c}^{\dagger}\right)\right] \tag{55}$$

where $\Omega_{R;j\alpha} = \frac{\mathbf{d}_{\alpha j}\cdot\mathbf{E}}{\hbar}$.

It is again convenient to work in the interaction picture where

$$\hat{H} = -\hbar\sum_{j=1}^{J}\sum_{\alpha=1}^{A}\Omega_{R;j\alpha}\hat{a}_j^{\dagger}\hat{a}_\alpha\hat{c}e^{i\Delta_{j\alpha}t} + \text{h.c.} \tag{56}$$

where $\Delta_{j\alpha} = \omega_{j\alpha} - \omega$. Note that the electric-dipole-forbidden transitions are eliminated by values $d_{j\alpha} = 0$.

Instead of the excitation and deexcitation operators for a qubit that are specific to a two-level system, $\hat{\sigma}^{\dagger}$and $\hat{\sigma}$, it is easier to introduce standard creation and annihilation operators of the fermion states. Therefore, the states that were denoted as $|0_{j\alpha}\rangle$ and $|1_{j\alpha}\rangle$ when using the operators $\hat{\sigma}^{\dagger}$ and $\hat{\sigma}$ become $|0_j\rangle\,|1_\alpha\rangle$ and $|1_j\rangle\,|0_\alpha\rangle$ when using standard fermion operators.

We consider again lowest-energy states corresponding to zero- or single-photon excitations:

$$\begin{aligned}\Psi = {} & C_{00}\,|0\rangle\,\Pi_{j=1}^{J}\,|0_j\rangle\,\Pi_{\alpha=1}^{A}\,|1_\alpha\rangle + C_{10}\,|1\rangle\,\Pi_{j=1}^{J}\,|0_j\rangle\,\Pi_{\alpha=1}^{A}\,|1_\alpha\rangle \\ & + \sum_{j,\alpha}^{N,A} C_{0j\alpha}\,|0\rangle\,|1_j\rangle\,|0_\alpha\rangle\,\Pi_{m\neq j}^{J}\,|0_m\rangle\,\Pi_{\beta\neq\alpha}^{A}\,|1_\beta\rangle\,.\end{aligned} \tag{57}$$

Equations for the probability amplitudes C_{10} and $C_{0j\alpha}$ within the stochastic Schrödinger equation formalism become

$$\dot{C}_{10} + \frac{\mu}{2}C_{10} - i\sum_{j=1}^{J}\sum_{\alpha=1}^{A}\Omega_{R;j\alpha}^{*}C_{0j\alpha}e^{-i\Delta_{j\alpha}t} = 0, \tag{58}$$

$$\dot{C}_{0j\alpha} - i\Omega_{R;j\alpha}C_{10}e^{i\Delta_{j\alpha}t} = 0. \tag{59}$$

If spin states are degenerate, pairs $\{j,\alpha\}$ corresponding to different spin states $\{j_\downarrow,\alpha_\downarrow\}$ and $\{j_\uparrow,\alpha_\uparrow\}$ have to be taken into account separately in Eqs. (58) and (59).

To proceed, we assign the number $s = 1, ..., J \times A$ to each pair $\{j,\alpha\}$ and therefore reduce the problem to the one already solved in this section. The most interesting result, in our opinion, is still the formation of a long-lived entangled dark state decoupled from the cavity field when the collective Rabi frequency $\left(\sum_{j=1}^{J}\sum_{\alpha=1}^{A}|\Omega_{R;j\alpha}|^2\right)^{1/2}$ exceeds the width of the inhomogeneous broadening $|\Delta_{j\alpha}|_{max}$.

VI. NONCLASSICAL MULTIPHOTON STATES IN DISSIPATIVE STRONGLY-COUPLED SYSTEMS

Many of the results obtained in previous sections for single-photon excitations, in particular the formation of dark entangled qubit states decoupled from the cavity field, can be generalized to arbitrary multiphoton excitations which correspond to $N \geq M$ and $M > 1$ in Eqs. (4) and (6). To avoid cumbersome algebra, consider an example of equal Rabi frequencies and exact resonance, when one can put $\Omega_{Rj} = \Omega_R$ and $\Delta_j = 0$ in the Hamiltonian (3). This is not a critical assumption and it can be avoided at the expense of more complicated final expressions. Within the stochastic equation for the state vector, any group of probability amplitudes with a fixed value of $M = n + p$ is described by the following system of equations,

$$\left(\frac{d}{dt} + \gamma_{np\alpha_p}\right)C_{np\alpha_p} - i\left(\Omega_R\sqrt{n+1}\sum_{\alpha_{p-1}}^{p}C_{(n+1)(p-1)\alpha_{p-1}} + \Omega_R^{*}\sqrt{n}\sum_{\alpha_{p+1}}^{N-p}C_{(n-1)(p+1)\alpha_{p+1}}\right) = \mathfrak{R}_{np\alpha_p}(t), \tag{60}$$

where

$$\overline{\mathfrak{R}_{np\alpha_p}(t)\mathfrak{R}_{n'p'\alpha_p'}^{*}(t')} = \hbar^2\delta(t-t')D_{np\alpha_p;n'p'\alpha_p'}. \tag{61}$$

The lower index in the sums shows the type of a subset and the upper index shows the number of elements in the sum. Equation (60) implies that the subsets α_{p-1} and α_{p+1} are related to subset α_p through

$$|p,\alpha_p\rangle = \hat{\sigma}^{\dagger}_{j_{p-1}}|p-1,\alpha_{p-1}\rangle\,,\ |p,\alpha_p\rangle = \hat{\sigma}_{j_{p+1}}|p+1,\alpha_{p+1}\rangle \tag{62}$$

where each pair α_p,α_{p-1} or α_p,α_{p+1} corresponds to a certain value of the qubit index: j_{p-1} or j_{p+1}. Each subset α_p corresponds to a certain finite number of subsets α_{p-1} or α_{p+1} which contribute to the summation in Eq. (60).

In the general case the presence of noise source terms $\mathfrak{R}_{np\alpha_p}$ couples the groups with different values of M. However, in the strong coupling regime such a noise-induced coupling scales as a small parameter $\frac{\gamma_{np\alpha_p}}{\Omega_R} \ll 1$ and therefore can be included perturbatively. A similar perturbative approach has been developed for nonlinear strong coupling of electron-photon-phonon systems [56].

Furthermore, for high enough photon frequencies $\hbar\omega \gg T$, one can assume zero temperature of dissipative reservoirs. At optical frequencies this is true even at room temperature. In this case the method of determining relaxation rates $\gamma_{np\alpha_p}$ and correlators $D_{np\alpha_p;n'p'\alpha'_p}$ is described in Sec. III. Assuming in addition that field dissipation is dominant in a nanocavity, we obtain

$$\gamma_{np\alpha_p} = n\frac{\mu}{2}, \tag{63}$$

$$D_{np\alpha_p;n'p'\alpha'_p} = \langle n|\langle p,\alpha_p|\delta\hat{L}(\hat{\rho})_{\hat{\rho}=\overline{|\Psi\rangle\langle\Psi|}}|p',\alpha'_p\rangle|n'\rangle = \mu\delta_{pp'}\delta_{\alpha_p\alpha'_p}\sqrt{(n+1)(n'+1)}\times\overline{C_{(n+1)p\alpha_p}C^{*}_{(n'+1)p'\alpha'_p}}, \tag{64}$$

where the operator $\delta\hat{L}(\hat{\rho})$ is determined by the last term in Eq. (13). It follows from Eq. (64) that nonzero autocorrelators of noise terms inside the group with a fixed value of $M = n+p$ are determined by averages of the amplitudes $\overline{C_{(n+1)p\alpha_p}C^{*}_{(n+1)p\alpha_p}}$ from the group with $M \Rightarrow M+1$:

$$D_{np\alpha_p;np\alpha_p} = \mu(n+1)\overline{C_{(n+1)p\alpha_p}C^{*}_{(n+1)p\alpha_p}};$$

whereas, nonzero cross-correlators coupling the groups with different $M = n+p$ and $M' = n'+p'$ are determined by the amplitudes $\overline{C_{(n+1)p\alpha_p}C^{*}_{(n'+1)p\alpha_p}}$ from the groups with $M \Rightarrow M+1$ and $M' \Rightarrow M'+1$:

$$D_{np\alpha_p;n'p\alpha_p} = \mu\sqrt{(n+1)(n'+1)}\overline{C_{(n+1)p\alpha_p}C^{*}_{(n'+1)p\alpha_p}}.$$

Therefore, for low-temperature reservoirs the coupling between blocks with different M exists only in the downward direction. The maximum value of M is determined by the initial energy of the system; thermal excitations above initial M are impossible. Within the group corresponding to maximum M all correlators $\overline{\mathfrak{R}_{np\alpha_p}(t)\mathfrak{R}^{*}_{n'p'\alpha'_p}(t')}$ are equal to zero and therefore one can neglect the noise terms in Eq. (60) for this group as they do not affect the observables. The noise terms in lower-M groups affect how the deexcitation proceeds across all possible relaxation channels (as, e.g., in [56]). At the same time the relaxation rate of the states in the highest-M group is determined only by the values of $\gamma_{np\alpha_p} = n\frac{\mu}{2}$.

These properties allow us to obtain intuitive analytic results describing quantum dissipative multiqubit dynamics at low reservoir temperature. For example, consider the states in the highest-M group where we can put $\mathfrak{R}_{np\alpha_p} = 0$ in Eq. (60) and take into account Eq. (63). This gives

$$\begin{array}{c}\left(\frac{d}{dt} + n\frac{\mu}{2}\right)C_{n(M-n)\alpha_{M-n}} - i\left(\Omega_R\sqrt{n+1}\sum\nolimits_{\alpha_{M-n-1}}^{M-n} C_{(n+1)(M-n-1)\alpha_{M-n-1}}\right. \\ \left. +\Omega^{*}_R\sqrt{n}\sum\nolimits_{\alpha_{M-n+1}}^{N-M+n} C_{(n-1)(M-n+1)\alpha_{M-n+1}}\right) = 0,\end{array} \tag{65}$$

where $n = 0,1,...,M$.

The main technical difficulty with solving Eqs. (65) is related to the rules imposed by Eq. (62),which dictate how each element of the subset α_{M-n} is related to the elements of subsets $\alpha_{M-n\mp1}$ which enter the sums $\sum_{\alpha_{M-n-1}}^{M-n}(...)$ and $\sum_{\alpha_{M-n+1}}^{N-M+n}(...)$, respectively. However, one avoids this complication when finding complex energy eigenvalues by summing each of Eqs. (65) over all subsets α_{M-n}. This results in the following equations for the variables

$$F_n = \sum_{\alpha_{M-n}}^{\mathcal{C}_N^{M-n}} C_{n(M-n)\alpha_{M-n}}:$$

$$\left(\frac{d}{dt}+n\frac{\mu}{2}\right)F_n - i\left(\Omega_R\sqrt{n+1}(N-M+n+1)F_{n+1}+\Omega_R^*\sqrt{n}(M-n+1)F_{n-1}\right)=0. \tag{66}$$

For example, consider the case of $M=2$. Seeking $F_n \propto e^{\Gamma t}$ we obtain

$$\begin{pmatrix} \Gamma & -i(N-1)\Omega_R & 0 \\ -i2\Omega_R^* & \Gamma+\frac{\mu}{2} & -i\sqrt{2}\Omega_R \\ 0 & -i\sqrt{2}\Omega_R^* & \Gamma+\mu \end{pmatrix}\begin{pmatrix} F_0 \\ F_1 \\ F_2 \end{pmatrix}=0, \tag{67}$$

which gives

$$\Gamma\left(\Gamma+\frac{\mu}{2}\right)(\Gamma+\mu)+2N|\Omega_R|^2\Gamma+2(N-1)|\Omega_R|^2\mu=0. \tag{68}$$

When $N\gg 1$, equation (68) can be factorized:

$$(\Gamma+\mu)\left[\Gamma\left(\Gamma+\frac{\mu}{2}\right)+2N|\Omega_R|^2\right]=0,$$

which gives

$$\Gamma_{1,2}\approx -\frac{\mu}{4}\pm i\left(2N|\Omega_R|^2-\frac{\mu^2}{16}\right)^{1/2},\ \Gamma_3\approx-\mu. \tag{69}$$

It is easy to see that the roots $\Gamma_{1,2}$ describe evolution of coupled 1-photon and 0-photon states,

$$\Psi_{n=0,1}=\Psi_{n=0}+\Psi_{n=1}=\sum_{\alpha_2}^{\mathcal{C}_N^2}C_{02\alpha_2}|0\rangle|2,\alpha_2\rangle+\sum_{\alpha_1}^{\mathcal{C}_N^1}C_{11\alpha_1}|1\rangle|1,\alpha_1\rangle,$$

whereas root Γ_3 describes evolution of the 2-photon state,

$$\Psi_{n=2}=C_{20\alpha_0}|2\rangle|0,\alpha_0\rangle,\ \text{where}\ |0,\alpha_0\rangle\equiv|0_{qub}\rangle.$$

Therefore, for a large number of qubits the 2-photon state evolves independently of other states and decays with decay rate μ. At the same time, 1-photon and 0-photon states get entangled while oscillating with collective Rabi frequency $\approx\left(2N|\Omega_R|^2-\frac{\mu^2}{16}\right)^{1/2}$ and decay with decay rate $\frac{\mu}{4}$.

As the next example, we consider an initial state in which M qubits are excited whereas the cavity field is in the vacuum state, i.e., $\Psi^{(0)}=\sum_{\alpha_M}^{\mathcal{C}_N^M}C^{(0)}_{0M\alpha_M}|0\rangle|M,\alpha_M\rangle$. The superscript (0) denotes initial moment of time $t=0$. An arbitrary initial state is a superposition of bight and dark initial states. Let's consider their evolution separately.

A. Dark states

These are uncoupled from the cavity field and therefore are relatively long-lived, especially in the nanocavity QED context where the relaxation is dominated by the cavity field decay. The dark states must satisfy the conditions

$$\sum_{\alpha_M}^{N-M+1}C^{(0)}_{0M\alpha_M}=0. \tag{70}$$

Every element of the subset α_{M-1} in Eqs. (70) is related to the elements of subset α_M in the sum $\sum_{\alpha_M}^{N-M+1}(...)$ according to the rules of Eqs. (62). It is easy to see that an initial state vector which satisfies the conditions $C^{(0)}_{(n>0)(M-n)\alpha_{M-n}}=0$ and Eqs. (70) remains constant with time, i.e., is a stationary solution of Eqs. (65).

Equations (70) contain $\mathcal{C}_N^{M-1}$ equations for $\mathcal{C}_N^M$ variables, i.e., the dark state conditions can be satisfied when $\mathcal{C}_N^M>\mathcal{C}_N^{M-1}$. This gives the condition for the existence of dark states: not more than half of the qubits can be initially excited,

$$N\geq 2M. \tag{71}$$

The structure of a dark state can be visualized for a simple example, when $M = 2$ and $N = 4$. In this case the initial state vector is given by

$$\begin{aligned}\Psi^{(0)} = |0\rangle \Big(& C_{12}^{(0)}|1\rangle|1\rangle|0\rangle|0\rangle + C_{13}^{(0)}|1\rangle|0\rangle|1\rangle|0\rangle + C_{14}^{(0)}|1\rangle|0\rangle|0\rangle|1\rangle \\ & + C_{23}^{(0)}|0\rangle|1\rangle|1\rangle|0\rangle + C_{24}^{(0)}|0\rangle|1\rangle|0\rangle|1\rangle + C_{34}^{(0)}|0\rangle|0\rangle|1\rangle|1\rangle \Big),\end{aligned} \tag{72}$$

where the ket before the parentheses is the photon state. Equations (70) become

$$C_{12}^{(0)} + C_{13}^{(0)} + C_{14}^{(0)} = 0,\ C_{12}^{(0)} + C_{23}^{(0)} + C_{24}^{(0)} = 0,\ C_{13}^{(0)} + C_{23}^{(0)} + C_{34}^{(0)} = 0,\ C_{14}^{(0)} + C_{24}^{(0)} + C_{34}^{(0)} = 0,$$

which gives the dark state as

$$C_{12}^{(0)} = C_{34}^{(0)} = A,\ C_{13}^{(0)} = C_{24}^{(0)} = B,\ C_{14}^{(0)} = C_{23}^{(0)} = C, \tag{73}$$

and

$$A + B + C = 0. \tag{74}$$

Note that the dark states at any moment of time correspond to the trivial solution of Eqs. (66): $F_n = 0$ for any n. Therefore, they cannot be analyzed with Eqs. (66).

B. Bright states

Obviously, one of the bright states is a completely symmetric state:

$$C_{0M\alpha_M}^{(0)} = \text{const} = \frac{1}{\sqrt{\mathcal{C}_N^M}}. \tag{75}$$

In this case due to symmetry we have $C_{n(M-n)\alpha_{M-n}} = \frac{F_n}{\mathcal{C}_N^{M-n}}$ at any moment of time. Such states are typical for the systems possessing permutational symmetry [7]. Then from Eqs. (66) we obtain that there is only one stationary state $F_n = 0$ for any n, which means that the energy of the state satisfying Eq. (75) will be radiated away completely.

The state given by Eq. (75) is not the only bright state. Consider again the case of $M = 2$ and $N = 4$ for illustration. In this case the state vector at an arbitrary moment of time has the structure

$$\begin{aligned}\Psi = & |0\rangle \left(C_{12}|1\rangle|1\rangle|0\rangle|0\rangle + C_{13}|1\rangle|0\rangle|1\rangle|0\rangle + C_{14}|1\rangle|0\rangle|0\rangle|1\rangle + C_{23}|0\rangle|1\rangle|1\rangle|0\rangle + C_{24}|0\rangle|1\rangle|0\rangle|1\rangle + C_{34}|0\rangle|0\rangle|1\rangle|1\rangle\right) \\ & + |1\rangle \left(C_1|1\rangle|0\rangle|0\rangle|0\rangle + C_2|0\rangle|1\rangle|0\rangle|0\rangle + C_3|0\rangle|0\rangle|1\rangle|0\rangle + C_4|0\rangle|0\rangle|0\rangle|1\rangle\right) + |2\rangle C_0|0\rangle|0\rangle|0\rangle|0\rangle.\end{aligned} \tag{76}$$

Consider the following initial state: $C_{14}^{(0)} = -C_{23}^{(0)} \neq 0$, $C_{ij\neq 14,23}^{(0)} = 0$, $C_{1,2,3,4}^{(0)} = 0$, $C_0^{(0)} = 0$. One can show that in this case at any moment of time $C_{14} = -C_{23}$, $C_{ij\neq 14,23}^{(0)} = 0$, $C_1 = C_4 = -C_2 = -C_3$, $C_0 = 0$. As a result, Eqs. (65) yield the following equations,

$$\frac{d}{dt}C_{14} - 2i\Omega_R C_1 = 0,\ \left(\frac{d}{dt} + \frac{\mu}{2}\right) C_1 - i\Omega_R^* C_{14} = 0,$$

which describe decaying Rabi oscillations at frequency $\approx \left(2|\Omega_R|^2 - \frac{\mu^2}{16}\right)^{1/2}$ resulting in a complete radiative energy loss with amplitude decay rate $\frac{\mu}{4}$. Formally, these expressions for the decay rate and Rabi frequency obtained using Eqs. (65) are similar to those obtained from Eqs. (66). However, it is easy to see that the above solution corresponds to the trivial solution of Eqs. (66), i.e., $F_n = 0$ for all n, and therefore it cannot be derived from Eqs. (66).

Since the system is linear, an antisymmetric initial state of a more general form,

$$C_{12}^{(0)} = -C_{34}^{(0)},\ C_{13}^{(0)} = -C_{24}^{(0)},\ C_{14}^{(0)} = -C_{23}^{(0)},$$

is also bright.

It is easy to see that any initial state of the type Eq. (72) can always be split into two bright states (symmetric and antisymmetric one) and one dark state. For example, suppose that we initially excited one pair of qubits with

probability of 1, i.e., $\Psi^{(0)} = |0\rangle|1\rangle|1\rangle|0\rangle|0\rangle$, where as always the first ket describes the photon state. This state can be represented as a sum of a symmetric bright state,

$$\Psi^{(s)}_{bright} = \frac{1}{6}|0\rangle\left(|1\rangle|1\rangle|0\rangle|0\rangle + |1\rangle|0\rangle|1\rangle|0\rangle + |1\rangle|0\rangle|0\rangle|1\rangle + |0\rangle|1\rangle|1\rangle|0\rangle + |0\rangle|1\rangle|0\rangle|1\rangle + |0\rangle|0\rangle|1\rangle|1\rangle\right),$$

an asymmetric bright state,

$$\Psi^{(as)}_{bright} = \frac{1}{2}|0\rangle\left(|1\rangle|1\rangle|0\rangle|0\rangle - |0\rangle|0\rangle|1\rangle|1\rangle\right),$$

and a dark state,

$$\Psi_{dark} = \frac{1}{6}|0\rangle\left(2|1\rangle|1\rangle|0\rangle|0\rangle - |1\rangle|0\rangle|1\rangle|0\rangle - |1\rangle|0\rangle|0\rangle|1\rangle - |0\rangle|1\rangle|1\rangle|0\rangle - |0\rangle|1\rangle|0\rangle|1\rangle + 2|0\rangle|0\rangle|1\rangle|1\rangle\right).$$

One can see that 1/3 of the original excitation energy goes to the dark state and is preserved until the qubit decay kicks in. The fraction of the preserved excitation increases if the initial state is closer to the dark state. For example, an initial state $\Psi^{(0)} = \frac{1}{\sqrt{2}}|0\rangle\left(|1\rangle|1\rangle|0\rangle|0\rangle + |0\rangle|0\rangle|1\rangle|1\rangle\right)$ is a sum of a symmetric bright state,

$$\Psi^{(as)}_{bright} = \frac{1}{2\sqrt{2}}|0\rangle\left(|1\rangle|1\rangle|0\rangle|0\rangle + |1\rangle|0\rangle|1\rangle|0\rangle + |1\rangle|0\rangle|0\rangle|1\rangle + |0\rangle|1\rangle|1\rangle|0\rangle + |0\rangle|1\rangle|0\rangle|1\rangle + |0\rangle|0\rangle|1\rangle|1\rangle\right),$$

and a dark state,

$$\Psi_{dark} = \frac{1}{2\sqrt{2}}|0\rangle\left(|1\rangle|1\rangle|0\rangle|0\rangle - |1\rangle|0\rangle|1\rangle|0\rangle - |1\rangle|0\rangle|0\rangle|1\rangle - |0\rangle|1\rangle|1\rangle|0\rangle - |0\rangle|1\rangle|0\rangle|1\rangle + |0\rangle|0\rangle|1\rangle|1\rangle\right).$$

In this case 1/2 of the original excitation energy goes into the dark state.

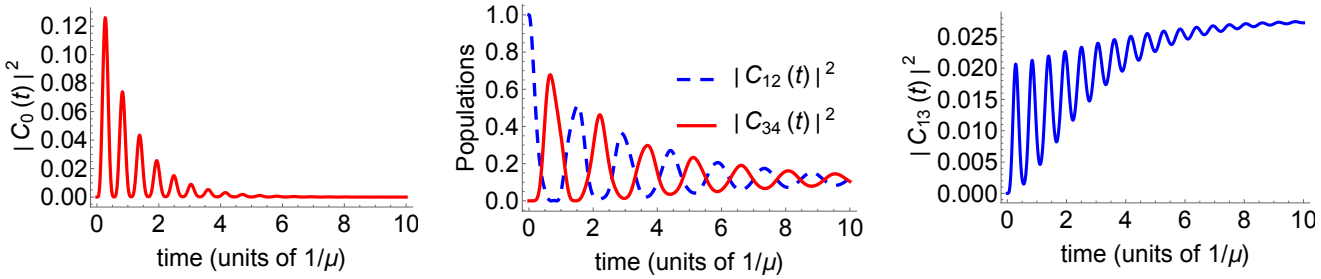

FIG. 7: An example of time evolution of populations for the $M = 2$, $N = 4$ state (76), when the two qubits are excited initially, namely $C_{12} = 1$ and all other coefficients are zero. The Rabi frequency Ω_R is 100 meV and cavity decay time $1/\mu = 20$ fs. Left panel: occupation probability of the two-photon state $|C_0(t)|^2$; middle panel: same for $|C_{12}(t)|^2$ and $|C_{34}(t)|^2$; right panel: same for $|C_{13}(t)|^2$. The dynamics of other $|C_{ij}(t)|^2$ probabilities looks similar to that of $|C_{13}(t)|^2$.

Figures 7 and 8 illustrate this dynamics with a numerical example by solving Eqs. (65) with the rules imposed by Eq. (62) for the initial state $\Psi^{(0)} = |0\rangle|1\rangle|1\rangle|0\rangle|0\rangle$ in which two qubits are excited with unit probability and all other coefficients are zero. This initial state is a mix of bright and dark states. As is clear from Fig. 7 plotted for the $M = 2$, $N = 4$ state given by Eq. (76), the bright state part is radiated away over the time of several $1/\mu$, after which all occupations containing one or two photons, namely $|C_j(t)|^2$ where $j = 0, 1, 2, 3, 4$, approach zero whereas all two-qubit coefficients approach an entangled dark state decoupled from the cavity mode, in which the sum of all qubit populations is equal to 1/3 as predicted by our analytic theory; see the dashed blue curve in Fig. 8.

With increasing total number of qubits N the fraction of the initial excitation which goes into the dark state increases rapidly, as illustrated with the $M = 2$, $N = 6$ example in Fig. 8; see the solid red curve. This behavior is qualitatively similar to the case of single-photon excitations solved in the main text.

If the experiment has a complete control over qubit excitations, one can switch between dark and bright states as needed; however, even in the case of no control the fact that a large or even dominant fraction of the initial excitation goes into a long-lived dark state makes low-Q plasmonic nanocavities more appealing for applications.

For large values of m and N the procedure of expanding an initial state into bright and dark states is unlikely to be simpler than direct solution of ordinary differential equations (65) obtained within the SSE method. However,

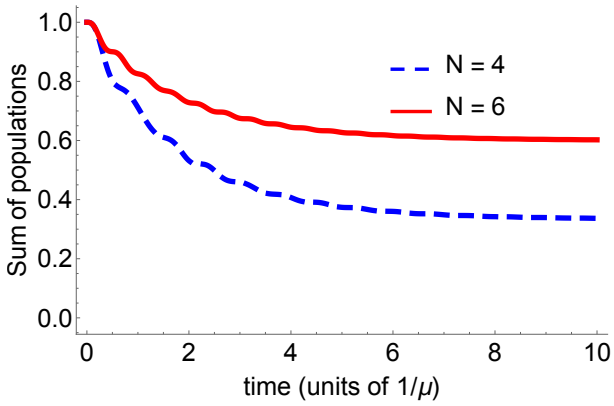

FIG. 8: Sum of all occupation probabilities for the $M = 2$, $N = 4$ state (76) (dashed blue curve) and the $M = 2$, $N = 6$ state (solid red curve) as a function of time, for the same initial conditions: two qubits are excited, namely $C_{12} = 1$ and all other coefficients are zero.

there is a class of initial states for which this procedure is still the simplest. Consider the subset of states which do not have any common qubit and denote it as $|M, \tilde{\alpha}_M\rangle$. There are obviously $L = \frac{N}{M}$ of such states and we consider only the excitations where L is integer. If only such states are excited initially and all initial amplitudes are the same and equal to $\frac{1}{\sqrt{L}}$, such states keep almost all their initial energy, especially for large $N - M \gg 1$: the amplitudes of states in $|M, \tilde{\alpha}_M\rangle$ approach $\frac{1}{\sqrt{L}}\frac{N-M}{N-M+1}$ whereas the amplitudes of all other states $|M, \alpha_M\rangle$ are excited from zero to the level of $\frac{1}{\sqrt{L}}\frac{1}{N-M+1}$.

VII. CONCLUSIONS

We found analytic solutions for the quantum dynamics of many-qubit systems strongly coupled to a quantized electromagnetic cavity mode, in the presence of decoherence and dissipation for both quantum emitters and cavity photons. Analytic or semi-analytic solutions are derived for a broad class of open quantum systems including identical qubits, an ensemble of qubits in a nonuniform nanocavity field with a broad distribution of coulping strengths and transition frequencies, and multi-level electron systems. The formalism is based on the stochastic equation of evolution for the state vector, within Markov approximation for the relaxation processes and rotating wave approximation with respect to the optical transition frequencies. Although the stochastic Schrödinger equation is typically used for numerical Monte-Carlo simulations, our version of this approach turned out to be convenient for the analytic theory.

We demonstrated in the analytic derivation that the interaction of an ensemble of qubits with a single-mode spatially nonuniform quantum field leads to entangled states of practical importance, with destructive or constructive interference between the qubits depending on the initial excitation. In particular, if one or a small fraction of qubits were excited initially whereas the field was in the vacuum state, the subsequent relaxation drives the whole ensemble of qubits into an entangled dark state which is completely decoupled from the leaky cavity mode, even though each qubit remains strongly coupled to the field. It is nontrivial that only a small fraction $1/N$ of the initial excitation energy is lost before the system goes into the dark state, where N is the number of qubits in the ground state.

We found the conditions in which strong coupling overcomes the spread of transition frequencies of an ensemble of qubits or a multi-electron system and leads to formation of a decoupled many-qubit dark state with conserved total excitation energy, despite quasi-chaotic oscillatory dynamics of individual qubits. We also studied the interplay of bright and dark states for multiphoton excitation energies and determined the conditions for the formation of decoupled dark states.

A potentially important effect not included in this paper is direct dipole-dipole coupling between neighboring qubits. Dipole-dipole interactions can affect both the relaxation rates of the qubits and the transition frequencies, which would change the numerical values of these phenomenological parameters, without affecting the results. At the same time, dipole-dipole coupling contributes an additional interaction term in the Hamiltonian which This affects the dynamics of entangled dark states and could be potentially utilized for manipulation of the quantum state and implementation of logic gates. This is an interesting topic for future work.

ACKNOWLEDGMENTS

This work has been supported in part by the Air Force Office for Scientific Research Grant No. FA9550-21-1-0272, National Science Foundation Award No. 1936276, and Texas A&M University through STRP, X-grant and T3-grant programs.

Appendix A: Spatial distribution of the electric field in a plasmonic nanocavity

In this section, we derive a representative example of the spatial distribution of the cavity field that we use in the numerical examples in this paper. We are interested in fields oscillating at optical frequencies in a plasmonic nanocavity. Consider for definiteness the nanocavity created by a metallic sphere in (sub)nm vicinity to the metallic substrate, as in strong coupling experiments with gold nanoparticles or in typical nanotip-based cavity QED experiments; see, e.g., [20, 22, 23, 25, 48, 51]. One can approximate the tip apex as a sphere, with the radius R and variable distance to the substrate. In the above experiments, the tip apex radius was 10-20 nm whereas the nanoparticle radius varied in broader limits 20-50 nm.

All plasmonic nanocavities demonstrated so far are leaky, i.e., the field emitted by the qubits is coupled to propagating EM modes of various kinds. Nevertheless, the spatial distribution of the electric field confined in the region much smaller than wavelength, for example in the near zone of the nanoparticles or in the nanogap between the tip and the substrate, can still be described in the quasielectrostatic approximation. Within our approach based on phenomenological relaxation rates, the losses due to coupling to radiating modes contribute to the overall cavity loss rate μ. A detailed modeling of cavity modes in lossy and leaky plasmonic nanocavities is outside the scope of this paper.

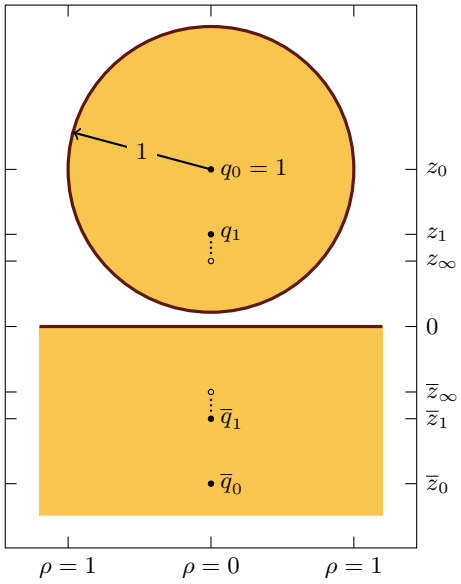

FIG. 9: To-scale diagram of the first four image charges for $z_0 = 1.1$ with all scales normalized to the radius of the sphere. Also shown are $z_\infty \equiv \lim_{n\to\infty} z_n$ and $\overline{z}_\infty \equiv \lim_{n\to\infty} \overline{z}_n$ (we calculate these in the text). No image charges are placed in the sphere below z_∞ and none are placed in the substrate above $\overline{z}_\infty$. The axes are the z and ρ of a cylindrical coordinate system.

We work in a cylindrical system of coordinates with the origin on the plane and the cylindrical axis—the z-axis—intersecting the center of a sphere at $z = z_0 > 0$. The placement of the coordinate system is illustrated in Fig. 9. We will normalize all spatial scales to the radius of the sphere. Since the sphere and the plane do not intersect, we have $z_0 > 1$. To find the spatial distribution of the nanocavity field, we assume both the nanosphere and the substrate to be perfect conductors. We solve the problem using the method of images, as suggested in [76]. Note that the method of images can be extended to materials with arbitrary complex dielectric permittivities; for example for a plane interface between the materials with dielectric permittivities ϵ_1 and ϵ_2 the image charge gets multiplied by the factor $\frac{\epsilon_1-\epsilon_2}{\epsilon_1+\epsilon_2}$ [77], which approaches the ideal conductor limit of -1 in the limit of large $|\epsilon_2| \gg 1$, no matter whether it is the real or imaginary part of the dielectric permittivity which has a large absolute value. For an interface with

a sphere the situation is more complicated as it requires summation over an infinite number of image charges, but again the corrective factor is an explicit function of dielectric constants and approaches the ideal conductor limit when the dielectric constant of a sphere $|\epsilon_2| \gg 1$; see [78]. If we take gold as an example [79], at near-infrared and longer wavelengths the Drude limit of $|\epsilon_2| \gg 1$ is valid. For example at the wavelength of 750 nm the dielectric constant of bulk gold is $\epsilon_2 \simeq -20 + 1.2i$ [79]. We numerically checked that for our geometry the resulting correction to the field amplitude as compared to an ideal conductor is less than 10 per cent at near-infrared and longer wavelengths. At visible and shorter wavelengths there will be a large deviation from the Drude limit, especially in the interband transition region. Furthermore, there will be plasmon resonances dependent on the cavity geometry.

Our problem, then, is that of solving the Laplace equation with Dirichlet boundary conditions on a sphere and a plane not intersecting the sphere. The geometry requires the placement of an infinite number of point charges along the z-axis. Without loss of generality, we suppose the sphere to be at some positive potential and the plane to be at a potential of zero. Note that here we are interested only in the spatial field distribution; the amplitude is determined by the normalization condition 1 for the quantized field mode.

First, we place an image charge q_0 at z_0—the center of the sphere; this raises the sphere to the desired nonzero potential. But q_0 breaks the boundary condition for the plane; the plane is distorted by q_0 to some nonzero, nonuniform potential. To restore the plane to ground, we place another image charge $\overline{q}_0 = -q_0$ at $\overline{z}_0 = -z_0$ inside the half-space—this is the reflection of q_0 in the plane. But now the boundary condition for the sphere is not satisfied. Typically, when it is introduced in elementary texts on electricity and magnetism (e.g., [77, 80, 81]), correcting the distortion on the plane by q_0 (a plane and a point charge) is the first problem solved via the method of images and correcting the distortion on the sphere by $\overline{q}_0$ (a sphere and a point charge) is the second. To cancel the effect of $\overline{q}_0$ on the sphere, we place q_1 at z_1 such that $(z_0 - z_1)(z_0 - \overline{z}_0) = 1$ and $q_1/\overline{q}_0 = -[(z_0 - z_1)/(z_0 - \overline{z}_n)]^{1/2}$. But now q_1 distorts the plane; so, we place $\overline{q}_1 = -q_1$ at $\overline{z}_1 = -z_1$, etc. The distortion of the plane by each q_n is canceled by $\overline{q}_n$, the reflection of q_n in the plane; the distortion of this $\overline{q}_n$ on the sphere is canceled by q_{n+1}, the reflection of $\overline{q}_n$ in the sphere. The first four image charges are depicted in Fig. 9.

In the following section, we write a set of coupled difference equations (or recursion relations) for the image charges and their positions on the z-axis; we solve these equations to obtain closed form expressions for q_n and z_n in terms of the initial conditions q_0 and z_0; then, we write the field on the metallic substrate—the location of the quantum emitters—as an infinite series where each term is the contribution from q_n and its reflection in the plane $\overline{q}_n$.

1. Series solution via difference equations

We set $q_0 = 1$, since the field amplitude is determined by normalization as already stated. Then we have

$$\overline{q}_n = -q_n, \tag{A1}$$

$$\overline{z}_n = -z_n, \tag{A2}$$

$$(z_0 - z_{n+1})(z_0 - \overline{z}_n) = 1, \tag{A3}$$

$$\begin{aligned} \frac{q_{n+1}}{\overline{q}_n} &= -\left(\frac{z_0 - z_{n+1}}{z_0 - \overline{z}_n}\right)^{1/2} \\ &= -\frac{1}{z_0 - \overline{z}_n}, \end{aligned} \tag{A4}$$

where the second line of Eq. (A4) follows from Eq. (A3) and the fact that $1/(z_0 - \overline{z}_n) > 0$. Decoupled and with the $\overline{q}_n$s and $\overline{z}_n$s eliminated, Eqs. (A1–A4) are

$$(z_0 - z_{n+1})(z_0 + z_n) = 1, \tag{A5}$$

$$\frac{1}{q_n} + \frac{1}{q_{n+2}} = \frac{2z_0}{q_{n+1}}. \tag{A6}$$

Eq. (A6) is solved in [76] but Eq. (A5) is not; we present solutions to both equations. The solution we present to Eq. (A6) is similar to the solution in [76].

Eq. (A6) is a second-order, linear difference equation in $1/q_n$; furthermore, the zeroth $(1/q_n)$ and second $(1/q_{n+2})$ terms are both multiplied by the same coefficient, namely, 1. The solutions to this kind of equation are nicely expressed in terms of hyperbolic functions; this is due to the following two identities for hyperbolic functions:

$$\begin{aligned} \sinh \vartheta n + \sinh \vartheta(n+2) &= 2\cosh\vartheta \sinh\vartheta(n+1), \\ \cosh \vartheta n + \cosh \vartheta(n+2) &= 2\cosh\vartheta \cosh\vartheta(n+1). \end{aligned} \tag{A7}$$

Since sinh and cosh are linearly independent, Eq. (A7) implies that

$$1/q_n = A\sinh\alpha n + B\cosh\alpha n, \tag{A8}$$

where α defined by

$$\cosh\alpha = z_0 \tag{A9}$$

is the general solution to Eq. (A6). The constants A and B can be determined from the given initial conditions q_0 and z_0. We use Eq. (A4) to find that $1/q_1 = 2z_0 = 2\cosh\alpha$; thus, A and B are determined by the system

$$\begin{aligned} 1/q_0 &= 1 = A, \\ 1/q_1 &= 2\cosh\alpha = A\cosh\alpha + B\sinh\alpha. \end{aligned} \tag{A10}$$

Eq. (A10) is solved by $A = 1$ and $B = 1/\tanh\alpha$; so, the image charges are given by

$$q_n = \frac{\sinh\alpha}{\sinh\alpha(n+1)}. \tag{A11}$$

In writing Eq. (A11), we have used the identity

$$\sinh\vartheta\cosh\varphi + \cosh\vartheta\sinh\varphi = \sinh(\vartheta+\varphi) \tag{A12}$$

to simplify the expression obtained from substituting the values of A and B found from solving Eq. (A10) into Eq. (A8).

We have obtained a closed-form expression for q_n; now, we turn our attention toward doing the same for z_n. While Eq. (A5) is nonlinear, it is first-order and rational; furthermore, it is of a form such that it can be reduced to a linear second-order difference equation via a simple nonlinear change of variable—this method is detailed in [82]. We rearrange Eq. (A5) by solving for z_{n+1} and adding $z_0 = \cosh\alpha$ to both sides:

$$z_{n+1} + \cosh\alpha = 2\cosh\alpha - \frac{1}{z_n + \cosh\alpha}. \tag{A13}$$

We write Eq. (A13) in terms of the new variable ξ_n where the ξ_ns are defined by $z_n + \cosh\alpha = \xi_{n+1}/\xi_n$; this leads to

$$\xi_{n+2} + \xi_n = 2\cosh\alpha\,\xi_{n+1}. \tag{A14}$$

Eq. (A14) is identical to Eq. (A6); so, Eq. (A14) is also solved by Eq. (A8), which implies

$$z_n + \cosh\alpha = \frac{\cosh\alpha(n+1) + C\sinh\alpha(n+1)}{\cosh\alpha n + C\sinh\alpha n}. \tag{A15}$$

Note that Eq. (A15) contains only one undetermined constant while Eq. (A8)—from which Eq. (A15) is derived—contains two. This is due to the fact that Eq. (A15) is the general solution to Eq. (A5), which is first-order, while Eq. (A8) is second-order.

Applying the initial condition $z_0 = \cosh\alpha$ to Eq. (A15) yields $C = 1/\tanh\alpha$ which leads to

$$z_n = \frac{\sinh\alpha}{\tanh\alpha(n+1)}. \tag{A16}$$

To obtain Eq. (A16), we have again used Eq. (A12) to simplify.

Using the expressions obtained for q_n and z_n, we can write the field $\mathbf{E}$ as an infinite series; but first, we consider the asymptotic behaviors of q_n and z_n for large n. Since, for large n, $\sinh\alpha(n+1)$ behaves like $e^{|\alpha|n}$, q_n rapidly approaches 0. On the other hand, z_n rapidly approaches the constant $|\sinh\alpha|$ since $\tanh\alpha(n+1)$ rapidly approaches 1 if $\alpha > 0$ or -1 if $\alpha < 0$. Denote

$$z_\infty \equiv \lim_{n\to\infty} z_n = |\sinh\alpha| = (z_0^2 - 1)^{1/2}. \tag{A17}$$

The last equality follows from the identity $\sinh\operatorname{arcosh} x = (x^2-1)^{1/2}$ which holds for all x such that $|x| > 1$. Since $z_\infty = (z_0^2-1)^{1/2}$, $z_\infty > z_0 - 1$ (i.e., the point $z = z_\infty$ on the z-axis is inside the ball) follows from the triangle

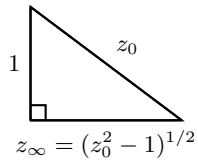

FIG. 10: The existence of a triangle with sides of these lengths is ensured by the Pythagorean theorem. The triangle inequality applied to this triangle yields $1 + (z_0^2 - 1)^{1/2} > z_0$; so, $z_\infty > z_0 - 1$. See Eq. (A17).

inequality—see Fig. 10; so, all image charges are placed inside one of the conductors (z_n strictly decreases from z_0 as n increases so $z_0 \geq z_n > z_\infty$ for all n), as expected.

We are interested in the field $\mathbf{E}$ in the $z = 0$ plane. In this plane we have

$$\begin{aligned}\mathbf{E} &= \sum_{n=0}^{\infty} \left[\frac{q_n(\boldsymbol{\rho} - \hat{\mathbf{z}} z_n)}{(\rho^2 + z_n^2)^{3/2}} - \frac{q_n(\boldsymbol{\rho} + \hat{\mathbf{z}} z_n)}{(\rho^2 + z_n^2)^{3/2}} \right] \\ &= -2\hat{\mathbf{z}} \sum_{n=0}^{\infty} \frac{q_n z_n}{(\rho^2 + z_n^2)^{3/2}}. \end{aligned} \tag{A18}$$

Since the field in the plane, as computed with Eq. (A18), is purely in the z direction, we will from now on write the magnitude of the field $E = -E_z$ instead of the field $\mathbf{E}$; also, since we are going to normalize the field, we drop the prefactor of 2 on the second line of Eq. (A18). Substituting Eqs. (A11) and (A16) into Eq. (A18), we arrive at

$$E_N \equiv \sinh^2 \alpha \sum_{n=1}^{N} \frac{\cosh \alpha n}{\sinh^2 \alpha n} \left[\rho^2 + \left(\frac{R \sinh \alpha}{\tanh \alpha n} \right)^2 \right]^{-3/2} \to E \text{ as } N \to \infty. \tag{A19}$$

For large n, the nth term in Eq. (A19) is proportional to $e^{-|\alpha| n}$; the series converges rapidly—more rapidly for larger values of $|\alpha|$, that is, for larger values of z_0 ($\cosh x$ is increasing on $x \in (0, \infty)$). Consider Fig. 11 which illustrates convergence of the series for the case $z_0 = 1.1$; E_N does not change appreciably between $N = 20$ and $N = 10^4$. Furthermore, for $z_0 \geq 2$ it is enough to have $N = 3$.

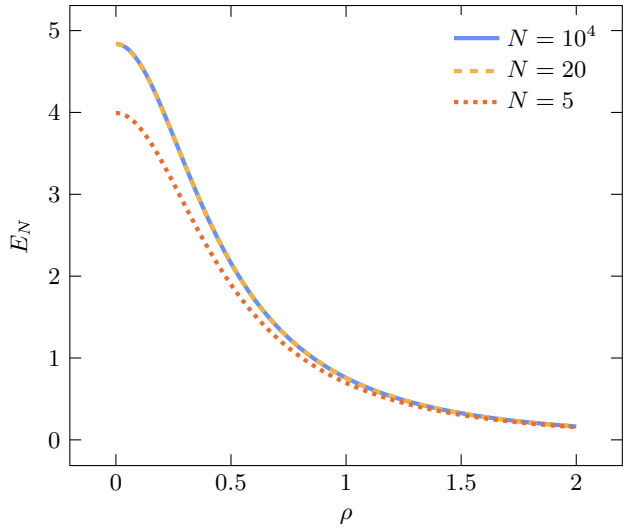

FIG. 11: E_N plotted against ρ for $z_0 = 1.1$ and various values of N. E_N is the field due to the first $2N$ image charges; it is the first N terms in the series solution for the field—Eq. (A19). The lines corresponding to E_{20} and E_{10^4} are indistinguishable. All fields are normalized to the same scale defined by placing the unit charge $q_0 = 1$ in the middle of the sphere and normalizing all distances by the radius of the sphere.

2. Two approximations

Equation (A19) is straightforward to use in numerical simulation but is unwieldy for the analytic derivation of the quantum dynamics in the main text. We consider two physically motivated approximations; we call one the *point-charge approximation* and the other the *line-charge approximation*.

We define the point-charge approximation

$$E_N^p \equiv \frac{Q_N Z_N}{(\rho^2 + Z_N^2)^{3/2}} \tag{A20}$$

where $Q_N \equiv \sum_0^{N-1} q_n$ and $Z_N \equiv (1/Q_N)\sum_0^{N-1} z_n q_n$. The point-charge approximation is the field due to a real dipole composed of Q_N at $z = Z_N$ and $-Q_N$ at $-Z_N$. By "real dipole" we mean two point charges with charges of opposite sign but equal magnitude separated by some finite distance. Unlike the field due to a dipole vector located at the origin, the field of this real dipole does not diverge for small as $\rho \to 0$. Q_N is just the total sum of charges. Z_N is the average of the displacements of the charges weighted according to the magnitude of the charges, i.e., it is the position of the q_n's center of mass but with charge instead of mass. The point-charge approximation is the field due to the point charge which most closely resembles the infinite series of image charges above the substrate and that most-closely-resembling charge's reflection in the plane.

The line charge approximation is

$$E_N^l \equiv \frac{Q_N}{z_0 - \sqrt{z_0^2 - 1}} \left(\frac{1}{\sqrt{\rho^2 + z_0^2 - 1}} - \frac{1}{\sqrt{\rho^2 + z_0^2}} \right) \tag{A21}$$

where Q_N is the same as in the point-charge approximation. The line-charge approximation is the field due to a total charge of Q_N distributed uniformly over the line between z_n and z_∞ and the reflection of this object in the plane. We chose a uniform charge distribution not because the discrete distribution of image charges are well approximated by uniform continuous distribution—it is not—but because it is simple and because it leads to an integrand with a nice antiderivative. The line-charge approximation is the most straightforward way to include the fact that the q_n's are extended in the z-direction.

While the point-charge approximation is a single term, its dependence on z_0—through Z_N and Q_N—is not expressed in closed form. On the other hand, while the line-charge approximation is two terms, its dependence on z_0 is simpler; it still contains Q_N but does not contain Z_N. We will see that the line-charge approximation is also more accurate for $z_0 \sim 1$ which is our main interest.

Fig. 12 illustrates the accuracy of the point and line-charge approximations at three values of z_0. We evaluate the accuracy of the approximations by comparing them to E_{20} (since $N = 20$ is enough terms for the series to converge at $z_0 = 1.1$—see Fig. 11, it should also be enough for $z_0 = 1.2$ and $z_0 = 11$). The line-charge approximation is more accurate than the point-charge approximation for $z_0 \sim 1$. For $z_0 <\approx 1.2$ the line-charge approximation underestimates the field at small ρ and for $z_0 >\approx 1.2$ the line-charge approximation overestimates the field at small ρ. For large z_0 (e.g., the $z_0 = 11$ plot in Fig. 12), while the point-charge approximation has converged to the true field, the line-charge approximation hovers above the true field, that is, the line-charge approximation overestimates the field by about the same amount for all ρ. The origin of this hovering behavior becomes apparent when we consider the point-charge approximation of the line-charge approximation, i.e., an approximation of an approximation (and the point-charge approximation is appropriate for any distant-from-the-origin and localized charge distribution mirrored in the plane). The best fit point charge to the line of charge involved in the line-charge approximation is a charge located at the center of the line, that is, at $z = z_0 - (z_0 - z_\infty)/2$; however, this is slightly too close to the origin—for large z_0, the exact field is best approximated by a point charge at $z = z_0$. Fig. 13 corroborates this argument; it shows that, for $z_0 = 11$, when the substitution $z_0 \to z_0 + (z_0 - z_\infty)/2$ is made, the point and line-charge approximations agree.

Appendix B: The limit of a continuous spectrum of transition frequencies

Consider a large enough sample of qubits with a dense enough distribution of transition frequencies, so that the continuous distribution limit in Eq. (50) is justified. This is possible when

$$|\Omega_{Rj}| \gg \Delta_j - \Delta_{j\pm1}.$$

In the opposite limit the field is mostly coupled to one qubit closest to resonance.

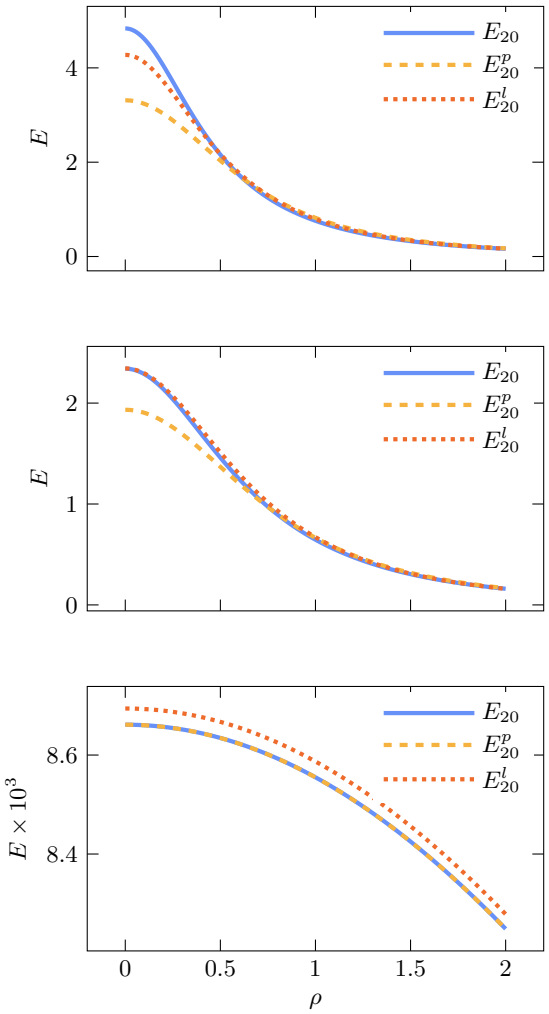

FIG. 12: Three plots of E_{20} (the series solution—Eq. (A19)), E^p_{20} (the point-charge approximation—Eq. (A20)) and E^l_{20} (the line-charge approximation—Eq. (A21)) against ρ for three values of z_0, namely, 1.1 (top panel), 1.2 (middle panel) and 11 (bottom panel). In the bottom panel, the lines corresponding to E_{20} and E^p_{20} are indistinguishable. All fields are normalized to the same scale described in the caption to Fig. 11. The numerical examples in the main text make use of the line approximation with $z_0 = 1.2$.

In the continuous limit we replace $\Delta_j \Rightarrow \Delta$ and introduce the density of states $g(\Delta)$ as

$$\sum_{j=k}^{k+p} O_j = \int_{\Delta_k}^{\Delta_{k+p}} O(\Delta) g(\Delta) d\Delta,$$

where O_j is a sequence of discrete values of a given function.

Then Eq. (50) is transformed as

$$\dot{C}_{10} + \frac{\mu}{2} C_{10} = i \int_{-\infty}^{\infty} e^{-i\Delta t} \Omega^*_{R\Delta} C_{0\Delta}(0) g(\Delta) d\Delta - \int_0^t \left[\int_{-\infty}^{\infty} e^{i\Delta(\tau - t)} |\Omega_{R\Delta}|^2 g(\Delta) d\Delta \right] C_{10}(\tau) d\tau. \tag{B1}$$

It is convenient to parameterize the density of states $g(\Delta)$ and $\Omega_{R\Delta}$ as

$$g(\Delta) = \frac{N}{2\Delta_m} f(\Delta), \ \Omega_{R\Delta} = \frac{\Omega_N}{\sqrt{N}} \rho(\Delta),$$

where $2\Delta_m$ is the width of the distribution of frequency detunings. With this parameterization $\int_{-\infty}^{\infty} f(\Delta) d\Delta = 2\Delta_m$.

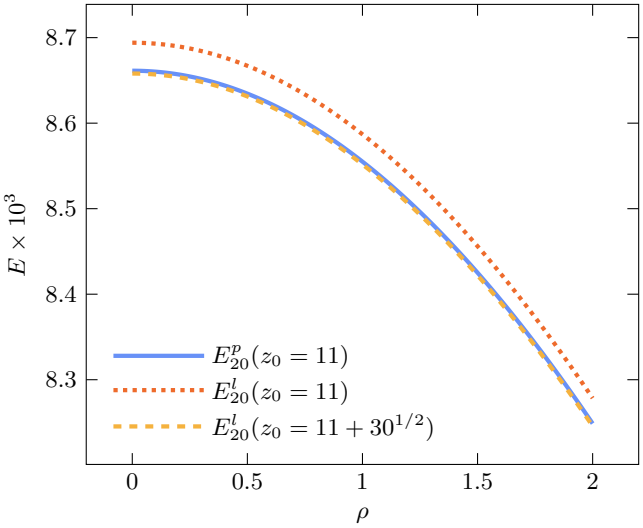

FIG. 13: Plot of the point-charge (Eq. (A20)) and line-charge (Eq. (A21)) approximations evaluated at $z_0 = 11$ as well as the line-charge approximation evaluated at $11 + [11 - (11^2 - 1)^{1/2}]/2 = 11 + 30^{1/2}$ against ρ. The lines correspond to $E^p_{20}(z_0 = 11)$ and $E^l_{20}(z_0 = 11 + 30^{1/2})$ are nearly indistinguishable. All fields are normalized to the same scale described in the caption to Fig. 11.

As a result, Eq. (B1) takes a form convenient for applying the Laplace transform:

$$\dot{C}_{10} + \frac{\mu}{2} C_{10} = i \frac{\sqrt{N}\Omega_N}{2\Delta_m} \tilde{F}(t) - \frac{|\Omega_N|^2}{2\Delta_m} \int_0^t \tilde{D}(t-\tau) C_{10}(\tau) d\tau, \tag{B2}$$

where

$$\tilde{F}(t) = \int_{-\infty}^{\infty} F_\Delta e^{-i\Delta t} d\Delta; \; F_\Delta = C_{0\Delta}(0)\rho^*(\Delta) f(\Delta);$$

$$\tilde{D}(t) = \int_{-\infty}^{\infty} D_\Delta e^{-i\Delta t} d\Delta; \; D_\Delta = |\rho(\Delta)|^2 f(\Delta).$$

Since $\int_{-\infty}^{\infty} |\Omega_{R\Delta}|^2 g(\Delta) d\Delta = \sum_{j=1}^{N} |\Omega_{Rj}|^2 = \Omega_N^2$, one can show that $\int_{-\infty}^{\infty} D_\Delta d\Delta = 2\Delta_m$.

Applying Laplace transform to Eq. (B2) gives

$$pC_p - C_{10}(0) + \frac{\mu}{2} C_p = i \frac{\sqrt{N}\Omega_N}{2\Delta_m} \tilde{F}_p - \frac{|\Omega_N|^2}{2\Delta_m} C_p \tilde{D}_p, \tag{B3}$$

where

$$\tilde{F}_p = \int_0^{\infty} \tilde{F}(t) e^{-pt} dt = \int_{-\infty}^{\infty} \frac{F_\Delta}{i\Delta + p} d\Delta,$$

$$\tilde{D}_p = \int_0^{\infty} \tilde{D}(t) e^{-pt} dt = \int_{-\infty}^{\infty} \frac{D_\Delta}{i\Delta + p} d\Delta.$$

Solving Eq. (B3) gives

$$C_{10}(t) = \frac{1}{2\pi i} \int_{x-i\infty}^{x+i\infty} \frac{C_{10}(0) + i\frac{\sqrt{N}\Omega_N}{2\Delta_m} \int_{-\infty}^{\infty} \frac{F_\Delta d\Delta}{i\Delta + p}}{p + \frac{\mu}{2} + \frac{|\Omega_N|^2}{2\Delta_m} \int_{-\infty}^{\infty} \frac{D_\Delta d\Delta}{i\Delta + p}} e^{pt} dp, \tag{B4}$$

where, as usual, the analytic continuation of the complex p-plane to the region $\mathrm{Re}[p] \leq 0$ corresponds to the counter-clockwise integration path around the poles in the integrals $\int_{-\infty}^{\infty} \frac{(\ldots) d\Delta}{i\Delta + p}$.

The poles of an integrand in Eq. (B4) are determined by

$$p + \frac{\mu}{2} + \frac{|\Omega_N|^2}{2\Delta_m}\int_{-\infty}^{\infty}\frac{D_\Delta}{i\Delta + p}d\Delta = 0. \tag{B5}$$

In our system the inhomogeneous broadening is much greater than the decay rate of the cavity field, $\Delta_m \gg \mu$; see Eq. (48). In the strong coupling regime, the Rabi frequency is also much greater than the cavity decay rate, $\Omega_N \gg \mu$. The value of the ratio between Δ_m and Ω_N determines two distinct dynamic regimes.

1. Strong inhomogeneous broadening

In this case

$$\frac{|\Omega_N|^2}{2\Delta_m^2} \ll 1 \ll \frac{N|\Omega_N|^2}{4\Delta_m^2}, \tag{B6}$$

where the second inequality is due to the limit of a continuous spectrum: the typical value of the Rabi frequency $\langle\Omega_R\rangle \sim \frac{\Omega_N}{\sqrt{N}}$ should exceed the distance between discrete spectral lines $2\Delta_m/N$. The first inequality ensures that near the pole the value of $|p| \sim \max\left[\mu, \frac{\Omega_N^2}{\Delta_m}\right] \ll \Delta_m$. In this case, taking into account correct direction of the integration path around the pole in Eq. (B4), we obtain a standard expression:

$$\frac{1}{i\Delta + p} \Rightarrow \pi\delta(\Delta) - i\frac{\mathcal{P}}{\Delta},$$

where $\mathcal{P}$ is principal value of the integral. The resulting solution of Eq. (B5) is

$$p_0 = -\frac{\mu}{2} - \frac{\pi|\Omega_N|^2}{2\Delta_m}D_{\Delta=0} + i\frac{|\Omega_N|^2}{2\Delta_m}\int_{-\infty}^{\infty}\frac{\mathcal{P}}{\Delta}D_\Delta d\Delta. \tag{B7}$$

It is easy to show that the expression $\frac{\pi|\Omega_N|^2}{2\Delta_m}D_{\Delta=0}$ is *exactly* the probability of transition per unit time from the state $|1\rangle\Pi_{j=1}^N|0_j\rangle$ into the continuous spectrum of states of excited qubits calculated with Fermi's Golden Rule.

The time evolution of $C_{10}(t)$ becomes

$$C_{10}(t) \approx \left[C_{10}(0) + \frac{\sqrt{N}\Omega_N}{2\Delta_m}\left(i\pi F_{\Delta=0} + \int_{-\infty}^{\infty}\frac{\mathcal{P}}{\Delta}F_\Delta d\Delta\right)\right]e^{p_0 t}. \tag{B8}$$

The second term in the brackets on the rhs of Eqs. (B8) is due to the dynamics at short times $t < \Delta_m^{-1} \ll \mu^{-1}$, i.e., before the exponential decay kicks in. If qubits are not initially excited, this term is exactly zero. Furthermore, it can be neglected if the initial probability of finding the photon mode excited, $P_{ph} = |C_{10}(0)|^2$, is at least as large as the initial excitation of the qubits, $P_{qub} = \sum_{j=1}^N |C_{0j}(0)|^2$, whereas the distribution of excitation probabilities of individual qubits is "uniform": $|F_\Delta| \sim |C_{0j}(0)| \sim \frac{1}{\sqrt{N}}|C_{10}(0)|$.

It is important to keep in mind that despite Eq. (48), dissipation of the cavity field can be faster than the energy transfer to resonant qubits, as long as

$$1 \gg \frac{\mu}{4\Delta_m} > \pi\frac{\Omega_N^2}{4\Delta_m^2}.$$

2. "Weak" inhomogeneous broadening

Now consider a relatively narrow frequency spectrum, when

$$\frac{\Omega_N^2}{2\Delta_m^2} \gg 1,$$

while still $\Delta_m \gg \mu$. In this case the transition to continuous spectrum is always valid and the roots of Eq. (B5) satisfy $|p| \sim \Omega_N \gg \Delta_m$. Since the typical width of the spectrum is $2\Delta_m$, we always have $D_{|\Delta|\sim\Omega_N \gg \Delta_m} \ll 1$, or even

$D_{|\Delta|>\Delta_m}=0$ for a limited spread of transition frequencies. Keeping only the leading nonzero terms with respect to a small parameter $\frac{\Delta_m}{\Omega_N}$ and using $\int_{-\infty}^{\infty}D_\Delta d\Delta=2\Delta_m$, Eq. (B5) can be transformed to

$$p^2+\Omega_N^2\approx-\left[\frac{\mu}{2}+\frac{\Omega_N^2}{2\Delta_m}\left(D_{\Delta=\mathrm{Im}[p]}-\frac{i}{p^2}\int_{-\infty}^{\infty}\Delta D_\Delta d\Delta+\frac{1}{p^3}\int_{-\infty}^{\infty}\Delta^2 D_\Delta d\Delta\right)\right]p, \tag{B9}$$

which has the solution

$$p_0=\pm i(\Omega_N-\delta\Omega_s)-i\delta\Omega_{as}-\kappa_\pm+o\left(\frac{(\delta\Omega_{s,as})^2}{\Omega_N},\frac{\kappa_\pm^2}{\Omega_N}\right), \tag{B10}$$

where

$$\delta\Omega_s=\frac{1}{4\Delta_m\Omega_N}\int_{-\infty}^{\infty}\Delta^2 D_\Delta d\Delta,\ \delta\Omega_{as}=-\frac{1}{2\Delta_m}\int_{-\infty}^{\infty}\Delta D_\Delta d\Delta,\ \kappa_\pm=\frac{\mu}{4}+\frac{\pi\Omega_N^2}{4\Delta_m}D_{\Delta=\pm\Omega_N}.$$

In particular, for Gaussian distribution $D_\Delta=\frac{2}{\sqrt{\pi}}e^{-\Delta^2/\Delta_m^2}$,

$$\delta\Omega_s=\frac{\Delta_m^2}{2\sqrt{\pi}\Omega_N},\ \delta\Omega_{as}=0,\ \kappa_+=\kappa_-=\frac{\mu}{4}+\frac{\sqrt{\pi}\Omega_N^2}{2\Delta_m}e^{-\Omega_N^2/\Delta_m^2}.$$

Note that the contribution to photon absorption $\kappa_\pm$ originated from light-qubit coupling (the second term) cannot be expanded in powers of a small parameter $\frac{\Delta_m}{\Omega_N}$.

Comparing this solution with the one obtained without any inhomogeneous broadening, it is easy to see that the frequency shift due to inhomogeneous broadening, $\sim\frac{\Delta_m^2}{\Omega_N}$, is always greater than the one due to finite cavity field decay, $\sim\frac{\mu^2}{\Omega_N}$, as long as Eq. (48) is satisfied. At the same time, photon absorption $\kappa_\pm$ is dominated by the cavity field dissipation μ. This is obvious when the spread of frequencies is limited and $D_{\Delta=\pm\Omega_N}=0$, but it remains true also for a Gaussian distribution D_Δ as long as

$$1\gg\frac{\mu}{4\Delta_m}>\frac{\sqrt{\pi}}{2}\frac{\Omega_N^2}{\Delta_m^2}e^{-\Omega_N^2/\Delta_m^2}.$$

To get simpler algebra, let's consider a symmetric distribution D_Δ when $\kappa_+=\kappa_-$ and $\delta\Omega_{as}=0$. A general case leads to more cumbersome expressions but the same qualitative result. Neglecting the terms of the order of $\frac{\int_{-\infty}^{\infty}\Delta F_\Delta d\Delta}{\Omega_N\int_{-\infty}^{\infty}F_\Delta d\Delta}\sim\frac{\Delta_m}{\Omega_N}$, $\frac{\int_{-\infty}^{\infty}\Delta^2 F_\Delta d\Delta}{\Omega_N^2\int_{-\infty}^{\infty}F_\Delta d\Delta}\sim\frac{\Delta_m^2}{\Omega_N^2}$, $\frac{\mu}{\Omega_N}$ etc., we obtain a result similar to the one for identical qubits without detunings. Indeed, in this case Eq. (B4) gives the following the solution for $C_{10}(t)$:

$$C_{10}(t)\approx\left(C_{10}(0)\cos\left[(\Omega_N-\delta\Omega_s)t\right]+i\frac{F(0)}{\Omega_N}\sin\left[(\Omega_N-\delta\Omega_s)t\right]\right)e^{-\kappa\tau}, \tag{B11}$$

where we used

$$\frac{\sqrt{N}\Omega_N}{2\Delta_m}\int_{-\infty}^{\infty}F_\Delta d\Delta=\sum_{j=1}^{N}\Omega_{Rj}^*C_{0j}(0)=F(0).$$

Substituting Eq. (B11) into Eq. (49) yields

$$C_{0j}(t)=C_{0j}(0)+i\Omega_{Rj}\int_0^t\left(C_{10}(0)\cos\left[(\Omega_N-\delta\Omega_s)t\right]+i\frac{F(0)}{\Omega_N}\sin\left[(\Omega_N-\delta\Omega_s)t\right]\right)e^{(i\Delta_j-\kappa)\tau}d\tau. \tag{B12}$$

[1] P. Törma and W. L. Barnes, Strong coupling between surface plasmon polaritons and emitters: a review, Rep. Prog. Phys. 78, 013901 (2015).

[2] P. Lodahl, S. Mahmoodian, and S. Stobbe, Interfacing single photons and single quantum dots with photonic nanostructures, Rev. Mod. Phys. 87, 347 (2015).

[3] C. L. Degen, F. Reinhard, and P. Cappellaro, Quantum sensing, Rev. Mod. Phys. 89, 035002 (2017).

[4] D. S. Dovzhenko, S. V. Ryabchuk, Yu. P. Rakovich, and I. R. Nabiev, Light-matter interaction in the strong coupling regime: configurations, conditions, and applications, Nanoscale 10, 3589 (2018).

[5] O. Bitton, S. N. Gupta, and G. Haran, Quantum dot plasmonics: from weak to strong coupling, Nanophotonics 8, 559 (2019).

[6] M. Tavis and F. W. Cummings, Exact solution for an N-molecule-radiation-field Hamiltonian, Phys. Rev. 170, 379-384 (1968).

[7] N. Shammah, S. Ahmed, N. Lambert, S. De Liberato, and F. Nori, Open quantum systems with local and collective incoherent processes: Efficient numerical simulations using permutational invariance, Phys. Rev. A 98, 063815 (2018).

[8] A. Laucht, J. M. Villas-Boas, S. Stobbe,3 N. Hauke, F. Hofbauer, G. Bohm, P. Lodahl, M.-C. Amann, M. Kaniber, and J. J. Finley, Mutual coupling of two semiconductor quantum dots via an optical nanocavity, Phys. Rev. B 82, 075305 (2010).

[9] M. Otten, R. A. Shah, N. F. Scherer, M. Min, M. Pelton, and S. K. Gray, Entanglement of two, three, or four plasmonically coupled quantum dots, Phys. Rev. B 92, 125432 (2015).

[10] M. Otten, J. Larson, M. Min, S. M. Wild, M. Pelton, and S. K. Gray, Origins and optimization of entanglement in plasmonically coupled quantum dots, Phys. Rev. A 94, 022312 (2016).

[11] P. Zoller and C. W. Gardiner. Quantum Noise in Quantum Optics: the Stochastic Schrödinger Equation. Lecture Notes for the Les Houches Summer School LXIII on Quantum Fluctuations in July 1995, Elsevier Science Publishers B.V. 1997, edited by E. Giacobino and S. Reynaud; arXiv:quant-ph/9702030v1.

[12] M. B. Plenio and P. L. Knight, The quantum-jump approach to dissipative dynamics in quantum optics, Rev. Mod. Phys. 70, 101 (1998).

[13] N. Gisin and I. C. Percival, The quantum-state diffusion model applied to open systems, J. of Phys. A: Mathematical and General 25 , 5677-5691 (1992).

[14] L. Diosi, N. Gisin, and W. T. Strunz, Non-Markovian quantum state diffusion, Phys. Rev. A 58, 1699-1712 (1998).

[15] C. Cohen-Tannoudji, B.o Zambon and E. Arimondo, Quantum-jump approach to dissipative processes: application to amplification without inversion, J. Opt. Soc. Am. B 10, 2107-2120 (1993).

[16] K. Molmer, Y. Castin and J. Dalibard, Monte Carlo wave-function method in quantum optics, J. Opt. Soc. Am. B 10, 524-538 (1993).

[17] N. Gisin and I. C. Percival, Wave-function approach to dissipative processes: are there quantum jumps? Phys. Lett. A 167, 315-318 (1992).

[18] M. Tokman, M. Erukhimova, Y. Wang, Q. Chen, and A. Belyanin, Generation and dynamics of entangled fermion-photon-phonon states in nanocavities, Nanophotonics 10, 491 (2021).

[19] Q. Chen, Y. Wang, S. Almutairi, M. Erukhimova, M. Tokman, and A. Belyanin. Dynamics and control of entangled electron-photon states in nanophotonic systems with time-variable parameters, Phys. Rev. A 103, 013708 (2021).

[20] R. Chikkaraddy, B. de Nijs, F. Benz, S. J. Barrow, O. A. Scherman, E. Rosta, A. Demetriadou, P. Fox, O. Hess, and J. J. Baumberg, Single-molecule strong coupling at room temperature in plasmonic nanocavities, Nature 535, 127 (2016).

[21] F. Benz, M. K. Schmidt, A. Dreismann, R. Chikkaraddy, Y. Zhang, A. Demetriadou, C. Carnegie, H. Ohadi, B. de Nijs, R. Esteban, J. Aizpurua, and J. J. Baumberg, Single-molecule optomechanics in picocavities, Science 354, 726 (2016).

[22] K.-D. Park, E. A. Muller, V. Kravtsov, P. M. Sass, J. Dreyer, J. M. Atkin, and M. B. Raschke, Variable-temperature tip-enhanced Raman spectroscopy of single-molecule fluctuations and dynamics, Nano Lett. 16, 479 (2016).

[23] H. Leng, B. Szychowski, M.-C. Daniel, and M. Pelton, Strong coupling and induced transparency at room temperature with single quantum dots and gap plasmons, Nat Commun. 9, 4012 (2018).

[24] H. Gross, J. M. Hamm, T. Tufarelli, O. Hess, and B. Hecht, Near-field strong coupling of single quantum dots, Sci. Adv. 2018; 4: eaar4906.

[25] K.-D. Park, M. A. May, H. Leng, J. Wang, J. A. Kropp, T. Gougousi, M. Pelton, M. B. Raschke, Tip-enhanced strong coupling spectroscopy, imaging, and control of a single quantum emitter, Sci. Adv. 2019;5: eaav5931.

[26] R. H. Dicke, Coherence in spontaneous radiation processes, Phys. Rev. 93, 99 (1954).

[27] M. Gross and S. Haroche, Superradiance: an essay on the theory of collective spontaneous emission, Phys. Rep. 93, 301 (1982).

[28] S. Schneider, and G. J. Milburn, Entanglement in the steady state of a collective-angular-momentum (Dicke) model, Phys. Rev. A 65, 042107 (2002).

[29] A. Gonzalez-Tudela and D. Porras, Mesoscopic entanglement induced by spontaneous emission in solid-state quantum optics, Phys. Rev. Lett. 110, 080502 (2013).

[30] M. O. Scully, Single photon subradiance: quantum control of spontaneous emission and ultrafast readout, Phys. Rev. Lett. 115, 243602 (2015).

[31] P. Kirton and J. Keeling, Suppressing and Restoring the Dicke Superradiance Transition by Dephasing and Decay, Phys. Rev. Lett. 118, 123602 (2017).

[32] Elie Wolfe and S. F. Yelin, Certifying Separability in Symmetric Mixed States of N Qubits, and Superradiance, Phys. Rev. Lett. 112, 140402 (2014).

[33] N. Shammah, N. Lambert, F. Nori, and S. De Liberato, Superradiance with local phase-breaking effects, Phys. Rev. A 96, 023863 (2017).

[34] M. Gegg, A. Carmele, A. Knorr and M. Richter, Superradiant to subradiant phase transition in the open system Dicke model: dark state cascades, New J. Phys. 20, 013006 (2018).

[35] A. Belyanin, V.V. Kocharovsky, Vl.V. Kocharovsky, Superradiant generation of femtosecond pulses in quantum-well heterostructures, Quant. & Semiclass. Opt. (JEOS Part B) 10, L13-L19 (1998).

[36] K. Cong, Q. Zhang, Y. Wang, G. T. Noe II, A. Belyanin, and J. Kono, Dicke superradiance in solids, JOSA B 33, C80

(2016).
[37] A. Pscherer, M.Meierhofer, D. Wang, Hr. Kelkar, D. Martin-Cano, T. Utikal ,S. Gotzinger, and V. Sandoghdar, Single-Molecule Vacuum Rabi Splitting: Four-Wave Mixing and Optical Switching at the Single-Photon Level, Phys. Rev. Lett. 127, 133603 (2021).
[38] G. Zengin, M. Wersäll, S. Nilsson, T. J. Antosiewicz, M. Kall, and T. Shegai, Realizing Strong Light-Matter Interactions between Single-Nanoparticle Plasmons and Molecular Excitons at Ambient Conditions, Phys. Rev. Lett. 114, 157401 (2015).
[39] T. Schwartz, J. A. Hutchison, C. Genet, and T.W. Ebbesen, Reversible Switching of Ultrastrong Light-Molecule Coupling, Phys. Rev. Lett. 106, 196405 (2011).
[40] P. A. Hobson, W. L. Barnesa, D. G. Lidzey, G. A. Gehring, D. M. Whittaker, M. S. Skolnick, S. Walker, Strong exciton–photon coupling in a low-Q all-metal mirror microcavity, Appl. Phys. Lett. 81, 3519 (2002).
[41] J. Heintz, N. Markesevic, E. Y. Gayet, N. Bonod, and S. Bidault, Few-Molecule Strong Coupling with Dimers of Plasmonic Nanoparticles Assembled on DNA, ACS Nano, 15, 14732 (2021).
[42] P. Geerlings, D. Berckmans, and H. P. Figeys, The influence of electrical and mechanical anharmonicity on the vibrational transition moments of diatomic and polyatomic molecules, J. of Molecular Structure 57, 283 (1979).
[43] R. Arul, D.n Grys, R. Chikkaraddy, N. S. Mueller, A. Xomalis, E. Miele, T. G. Euser, and J. J. Baumberg, Giant mid-IR resonant coupling to molecular vibrations in sub-nm gaps of plasmonic multilayer metafilms, Light 11, 281 (2022).
[44] T. Yoshie, A. Scherer, J. Hendrickson, G. Khitrova, H. M. Gibbs, G. Rupper, C. Ell, O. B. Shchekin, and D. G. Deppe, Vacuum Rabi splitting with a single quantum dot in a photonic crystal nanocavity, Nature 432, 200 (2004).
[45] J. P. Reithmaier, G. Sek, A. Loffler, C. Hofmann, S. Kuhn, S. Reitzenstein, L. V. Keldysh, V. D. Kulakovskii, T. L. Reinecke, and A. Forchel, Strong coupling in a single quantum dot - semiconductor microcavity system, Nature 432, 197 (2004).
[46] C. R. Kagan, L. C. Bassett, C. B. Murray, and S. M. Thompson, Colloidal Quantum Dots as Platforms for Quantum Information Science, Chem. Rev. 121, 3186 (2021).
[47] M. Pelton, S. D. Storm and H. Leng, Strong coupling of emitters to single plasmonic nanoparticles: exciton-induced transparency and Rabi splitting, Nanoscale 11, 14540 (2019).
[48] M. A. May, D. Fialkow, T. Wu, K.-D. Park, H. Leng, J. A. Kropp, T. Gougousi, P. Lalanne, M. Pelton, and Markus B. Raschke, Nano-Cavity QED with Tunable Nano-Tip Interaction, Adv. Quantum Technol. 3, 1900087 (2020).
[49] D. Wang, Cavity quantum electrodynamics with a single molecule: Purcell enhancement, strong coupling and single-photon nonlinearity, J. Phys. B: At. Mol. Opt. Phys. 54, 133001 (2021).
[50] D. Ratchford, F. Shafiei, S. Kim, S. K. Gray, and X. Li, Manipulating Coupling between a Single Semiconductor Quantum Dot and Single Gold Nanoparticle, Nano Lett. 11, 1049 (2011).
[51] M. May, T. Jiang, C. Du, K.-D. Park, X. Xu, A. Belyanin, and M. Raschke, Nanocavity clock spectroscopy: resolving competing exciton dynamics in WSe2/MoSe2 heterobilayers, Nano Lett. 21, 522 (2021).
[52] T. Wu, M. Gurioli, and P. Lalanne, Nanoscale Light Confinement: the Q's and V's, ACS Photonics 8, 1522 (2021).
[53] A. Manjavacas, P. Nordlander, and F. J. Garcia de Abajo, Plasmon blockade in nanostructured graphene, ACS Nano 6, 1724 (2012).
[54] Pai-Yen Chen, C. Argyropoulos, M. Farhat and J. S. Gomez-Diaz, Flatland plasmonics and nanophotonics based on graphene and beyond, Nanophotonics 6, 239 (2017).
[55] M.Tokman, Y. Wang, I. Oladyshkin, A. R. Kutayiah, and A. Belyanin, Laser-driven parametric instability and generation of entangled photon-plasmon states in graphene, Phys. Rev. B 93, 235422 (2016).
[56] M. Tokman, M. Erukhimova, Q. Chen, and A. Belyanin, The universal model of strong coupling at the nonlinear resonance in open cavity-QED systems, Phys. Rev. A 105, 053707 (2022).
[57] N. K. Langford, S. Ramelow, R. Prevedel, W. J. Munro, J. Milburn, and A. Zeilinger, Efficient quantum computing using coherent photon conversion, Nat. 478, 360 (2011).
[58] M. Reitz, C. Sommer, and C. Genes. Cooperative Quantum Phenomena in Light-Matter Platforms. PRX Quantum 3, 010201 (2022).
[59] K. Blum, *Density Matrix Theory and Applications* (Springer, Heidelberg, 2012).
[60] M. O. Scully and M. S. Zubairy, *Quantum Optics* (Cambridge University Press, Cambridge, 1997).
[61] C. Gardiner and P. Zoller, *Quantum Noise* (Springer-Verlag, Berlin, Heidelberg, 2004).
[62] M. Tokman, Z. Long, S. Al Mutairi, Y. Wang, M. Belkin, and A. Belyanin, Enhancement of the spontaneous emission in subwavelength quasi-two-dimensional waveguides and resonators, Phys. Rev. A 97, 043801 (2018).
[63] M. Tokman, Z. Long, S. AlMutairi, Y. Wang, V. Vdovin, M. Belkin, and A. Belyanin, Purcell enhancement of the parametric down-conversion in two-dimensional nonlinear materials, APL Photonics 4, 034403 (2019).
[64] V. M. Fain and Y. I. Khanin, *Quantum Electronics. Basic Theory* (Cambridge, MA, MIT, 1969).
[65] K. Bedingfield and A. Demetriadou, On the excitation and radiative decay rates of plasmonic nanoantennas, Nanophotonics 11 2271 (2022).
[66] K. H. Madsen and P. Lodahl, Quantitative analysis of quantum dot dynamics and emission spectra in cavity quantum electrodynamics, New J. of Phys. 15, 025013 (2013).
[67] L.D. Landau, E.M. Lifshitz, *Statistical Physics, Part 1* (Pergamon, Oxford, 1965).
[68] G. Khitrova, H. M. Gibbs, F. Jahnke, M. Kira, and S. W. Koch, Nonlinear optics of normal-mode-coupling semiconductor microcavities, Rev. Mod. Phys. 71, 1591 (1999).
[69] S. Dufferwiel, S. Schwarz, F. Withers, A.A.P. Trichet, F. Li, M. Sich, O. Del Pozo-Zamudio, C. Clark, A. Nalitov, D.D. Solnyshkov, G. Malpuech, K.S. Novoselov, J.M. Smith, M.S. Skolnick, D.N. Krizhanovskii1 and A.I. Tartakovskii,

Exciton–polaritons in van der Waals heterostructures embedded in tunable microcavities, Nature Comm. 6, 8579 (2015).
[70] Y. Todorov, A. M. Andrews, R. Colombelli, S. De Liberato, C. Ciuti, P. Klang, G. Strasser, and C. Sirtori, Ultrastrong Light-Matter Coupling Regime with Polariton Dots, Phys. Rev. Lett. 105, 196402 (2010).
[71] P. Forn-Diaz, L. Lamata, E. Rico, J. Kono, and E. Solano, Ultrastrong coupling regimes of light-matter interaction, Rev. Mod. Phys. 91, 025005 (2019).
[72] D. Ballarini and S. De Liberato, Polaritonics: from microcavities to sub-wavelength confinement, Nanophotonics 8, 641 (2019).
[73] Yungang Sang, Chun-Yuan Wang, Soniya S. Raja, Chang-Wei Cheng, Chiao-Tzu Huang, Chun-An Chen, Xin-Quan Zhang, Hyeyoung Ahn, Chih-Kang Shih, Yi-Hsien Lee, Jinwei Shi, and Shangjr Gwo, Tuning of Two-Dimensional PlasmonExciton Coupling in Full Parameter Space: A Polaritonic Non-Hermitian System, Nano Lett. 21, 2596 (2021).
[74] J. Qin, Yu-Hui Chen, Z. Zhang, Y. Zhang, R. J. Blaikie, B. Ding , and M. Qiu, Revealing Strong Plasmon-Exciton Coupling between Nanogap Resonators and Two-Dimensional Semiconductors at Ambient Conditions, Phys. Rev. Lett. 124, 063902 (2020).
[75] Z. He, Z. Han, J. Yuan, A. M. Sinyukov, H. Eleuch, C. Niu, Z. Zhang, J. Lou, J. Hu, D. V. Voronine, M. O. Scully, Quantum plasmonic control of trions in a picocavity with monolayer WS_2, Sci. Adv.5: eaau8763 (2019).
[76] W.R. Smythe, *Static and Dynamic Electricity*, 3rd ed. (McGraw-Hill, New York, 1968).
[77] L.D. Landau, E.M. Lifshitz, *Electrodynamics of Continuous Media*, 2nd ed. (Pergamon, Oxford, 1984).
[78] Z. Gan and Z. Xu, Multiple-image treatment of induced charges in Monte Carlo simulations of electrolytes near a spherical dielectric interface, Phys. Rev. B 84, 016705 (2011).
[79] R. L. Olmon, B. Slovick, T. W. Johnson, D. Shelton, Sang-Hyun Oh, G. D. Boreman, and M. B. Raschke, Optical dielectric function of gold, Phys. Rev. B 86, 235147 (2012).
[80] D.J. Griffiths, *Introduction to Electrodynamics*, 4th ed. (Cambridge University Press, Cambridge, 2017).
[81] J.D. Jackson, *Classical Electrodynamics*, 3rd ed. (John Wiley & Sons, Hoboken, 1999).
[82] L. Brand, A sequence defined by a difference equation, Am. Math. Mon., 62, 7, 489–492 (1955).